Ilmenites and their alteration products, sinkholes for uranium and radium in roll-front deposits after the example of South Tortkuduk (Kazakhstan)

Thomas Boulesteix, Michel Cathelineau, Etienne Deloule, Marc Brouand, Herve Toubon, Philippe Lach, Nicolas Fiet

▶ **To cite this version:**

Thomas Boulesteix, Michel Cathelineau, Etienne Deloule, Marc Brouand, Herve Toubon, et al.. Ilmenites and their alteration products, sinkholes for uranium and radium in roll-front deposits after the example of South Tortkuduk (Kazakhstan). Journal of Geochemical Exploration, 2019, 206, pp.106343. 10.1016/j.gexplo.2019.106343 . hal-02380982

HAL Id: hal-02380982
https://hal.science/hal-02380982

Submitted on 20 Jul 2022

HAL is a multi-disciplinary open access archive for the deposit and dissemination of scientific research documents, whether they are published or not. The documents may come from teaching and research institutions in France or abroad, or from public or private research centers.

L'archive ouverte pluridisciplinaire **HAL**, est destinée au dépôt et à la diffusion de documents scientifiques de niveau recherche, publiés ou non, émanant des établissements d'enseignement et de recherche français ou étrangers, des laboratoires publics ou privés.

Distributed under a Creative Commons Attribution - NonCommercial 4.0 International License

Version of Record: https://www.sciencedirect.com/science/article/pii/S0375674219300950
Manuscript_b0280f7477cb87fa2011367b0b84a9bc

Ilmenites and their alteration products, sinkholes for uranium and radium in roll-front deposits after the example of South Tortkuduk (Kazakhstan)

Boulesteix, T.; Cathelineau, M.; Deloule, E.; Brouand, M.; Toubon, H.; Lach, P.; Fiet, N.

Abstract

The approximate determination of average Ra/U disequilibria in orebodies is one of the most common causes of errors in U reserve estimations. In roll-front deposits, the disequilibria are however frequently distributed following complex geometries, which must be fully understood to prevent major U reserve overestimates and costly unproductive extractive operations. The processes responsible for disruption of the radioactive equilibria and the U and Ra carriers in such complex natural systems remain poorly constrained. In this contribution, we propose an innovative approach, mixing orebody to sub-grain scale studies to unravel the distribution of U and Ra and the processes responsible for their concentration and uncoupling.

Using mineral separations, gamma spectrometry and mineral-chemical analyses, we identified the Fe-Ti clusters (altered ilmenite + pyrite/marcasite) as the microsites for coffinite precipitation and Ra concentration. To understand the influence of such clusters on the distribution of U and Ra at the deposit scale, whole-rock Ra/U disequilibria were measured and mapped at a series of ten drill holes along a profile crosscutting the studied roll-front. The main Ra/U disequilibria are encountered around the mineralization in low U content zones. They are controlled by two main processes. (1) In the oxidized zones, the immobility of ^{230}Th with respect to the U produces patches of Ra disequilibria (carried by the altered U minerals). (2) In the immediate vicinity of the roll-front, the dissolution of the mineralization produces an Ra flux trapped by the alteration products of ilmenites, as definitely confirmed by direct SIMS measurements. Such a process is responsible for the Ra disequilibria envelope located downstream of the richest ores, also known as Ra halo. The highest Ra/U ratios correspond to oxidized upstream samples, but most other high Ra/U ratios are from reduced downstream samples close to the mineralization. Such a low to medium U content envelope with high Ra/U ratios constitutes the main cause of U reserve overestimations.

© 2019 published by Elsevier. This manuscript is made available under the CC BY NC user license
https://creativecommons.org/licenses/by-nc/4.0/

1. Introduction

Comprehensive assessment of Ra/U disequilibria is a key step towards the mastery of uranium resource estimation in roll-front deposits. Most of the current resource estimation strategies rely on estimations of orebody-scale average disequilibria to convert total gamma emissions into U contents. The approximate determination of average Ra/U ratios in rocks is however one of the most prominent causes of errors in U reserve estimation. Since complex Ra/U distributions may affect the quality of reserve estimates, the development of predictive models to locally adjust the mean disequilibrium to geological parameters would greatly enhance the accuracy of such estimations. However, the major processes responsible for the disruption of the radioactive equilibria and the U and Ra sinkholes in such complex natural systems remain poorly constrained.

Several scales of research are necessary to fully understand the processes, in particular in roll-front deposits: a) at the deposit scale, the U and Ra distributions within the main zones of the roll, i.e., the oxidized zone, the redox front, and the reduced zone, b) at the sample scale, sands mostly consist of quartz and feldspar grains, and most of the metal enrichments are concentrated onto organic matter fragments (Mathieu et al. 2015; Rallakis et al., 2019), pyrite (Ingham et al., 2014; Lach et al., 2015) or Fe-Ti oxides (Boulesteix et al., 2015; Mathieu et al., 2015).

In the studied orebodies from Kazakhstan, the main hosts of U ores are unconsolidated sands, deposited during fluvial flooding events (Munara, 2012). These sands contain heavy minerals such as Fe-Ti oxides, as placer accumulations (Munara, 2012; Boulesteix et al., 2015; Mathieu et al., 2015). Ilmenite is abundant in such facies, and when present its alteration products (pseudorutile, rutile, anatase) form the main nucleus for U and subsequently Ra trapping. At the sample scale, U distribution may be particularly complex, accompanying the formation of a series of pyrite types around altered ilmenite cores, with the same order of crystallization as in all the studied samples (Lach et al., 2015), over which U is deposited as P-coffinite, sometimes UO_2 spherolites (Lach et al., 2015; Mathieu et al., 2015). Such Fe-Ti clusters may be considered a favorable microsite for the formation of uranium ores, although the roll-front affects the facies, which exhibit different amounts of these minerals. The presence of ilmenite is therefore a key factor in the nucleation of coffinite, but its distribution does not control the shape of the roll-fronts.

At the secular equilibrium, the Ra distribution must follow the U distribution. Roll-fronts are however dynamic natural systems, where the secular equilibrium is rarely approached for the whole decay chains. Moreover, ^{238}U and ^{226}Ra have contrasting chemical behavior and half-lives, both intrinsically and with respect to the timescales of nuclide migration during the developmental history of active roll-fronts. The measured Ra/U disequilibria are then likely to arise from the uptake or lixiviation of both U and Ra, with very different implications for the roll-front evolution. The Ra/U ratio thus provides a snapshot of the local disequilibrium state but is of limited interest for the understanding of the geological processes underway. ^{230}Th is in an intermediate position in the ^{238}U decay chain between ^{234}U and its daughter nuclide ^{226}Ra, with an intermediate half-life of 75401 ± 300 yr (OECD/NEA Data Bank, 2009). ^{230}Th is considered only slightly soluble and almost immobile in natural waters (Langmuir and Herman, 1980; Chabaux et al., 2003). Therefore, combined with its chemical behavior during weathering, it constitutes at best an inertial reference indicative of eventual past nuclide activities or equilibria. Pairs of $^{238}U/^{230}Th$ and $^{230}Th/^{226}Ra$ ratios are thus of special interest to identify the processes responsible for breaking the equilibrium of the ^{238}U decay chain.

Uranium, radium and thorium are therefore good markers of the overall fractionation processes that affect the roll-front during its activity.

Since the main processes responsible for both the disruption of the radioactive equilibria and the U and Ra uptake in such complex natural systems remain poorly understood, the Ra/U anomalies were investigated using the example of a major roll-front in Kazakhstan (Fig. 1).

In this contribution, we propose an innovative approach mixing orebody to sub-grain scale studies to unravel U and Ra distribution and the processes responsible for their concentration and uncoupling. To do so, we took advantage of a series of ten drill holes distributed along a profile crosscutting the Muyunkum ore front (Fig. 1). The mineralogy and geochemistry of microsites particularly active in trapping U and Ra were explored, using a multi-technique approach. In addition, high resolution portable γ-spectrometry (HRpGS) and SIMS were applied to establish the distribution of ^{238}U, ^{230}Th and ^{226}Ra.

At the deposit scale, the uranium is depleted in the oxidized zone, whereas it is particularly enriched along the redox front. The disequilibria may thus follow complex geometries, which should be fully understood to prevent major uranium reserve overestimates.

2. Geological background

This study was focused on an orebody representative of the South Tortkuduk uranium deposits, which belongs to the Muyunkum field, one of the world-class roll-front type deposits of the Southern Kazakhstan province (Fig. 1). The Muyunkum deposit is located in the Chu Sarysu basin lying north of the NW-SE Karatau mountain range, which split the Syr-Darya basin after the Oligocene (Alexeiev et al., 2009; Dahlkamp, 2009; Bande et al., 2017). The sedimentary infill of the Chu-Sarysu basin, up to 2000 m thick at its center, is predominantly of continental origin with occasional shallow marine successions forming a number of clay barrier-bounded sandstone aquifers. Oxygenated groundwater fluxes, initiated by the Oligocene Tien Shan uplift, crossed the basin from the northern Kirgizian Range towards the NW and from the Aral Sea, imprinting the sediments with regional stacked epigenetic oxidation tongues (Fig. 2). Mainly consisting of pitchblende and coffinite (Mathieu et al., 2015; Hébert et al., 2019), mineralization occurs at the oxidation fronts, forming sinuous accumulations tens of meters wide and over hundreds of kilometers in length (Jaireth et al., 2008; Dahlkamp, 2009; Mathieu et al., 2015).

The Muyunkum field, located in the southern Chu-Sarysu basin (Fig. 1), was discovered and explored in the late 1970s and has been mined by Katco JV LLP since 2004 using the in-situ recovery technique. The world class Tortkuduk uranium deposit is hosted in two Eocene-aged, continental medium- to fine-grained arenitic-arkosic sand formations with a low clay content (typically 6-7 wt.%; Herbert et al., 2015), the Uyuk (lower) and Ikansk (upper) reservoirs (Boulesteix et al., 2015; Mathieu et al., 2015). The detailed mineralogy and petrography of these formations has been described in Munara (2012) and Mathieu et al. (2015). The isotopic ages obtained for the mineralization (Mikhailov and Petrov 1998; Mathieu et al., 2015) range up to the Late Miocene (2-20 Ma) and suggest a number of U remobilization episodes at the still currently active oxidation front.

3. Samples and methods

a. Samples

Thirty-eight samples were taken along the “600-PA” reference profile across a typical oxidation front of the 17y deposit (Fig. 2) and selected to study the spatial distribution of the Ra/U disequilibrium. Most of them are more or less consolidated, reduced, medium- to fine-grained gray sands, with an activity between 90 and 2500 c/s measured with a portable prospecting γ scintillometer (SPPγ) (Table 1). Two additional radiometric anomalies in oxidized sands (160 - 170 c/s) and three samples from the lower clay boundary (160 - 260 c/s) were recovered to further depict the Ra distribution in the roll-front cross-section. This selection of samples is representative of the various deposition and redox conditions (oxidized/reduced, nose/wings, lenses) along the roll-front (Table 1; Fig. 2). Five other samples with a severe level of Ra disequilibria, representative of the orebody sandstones, were specially collected from an exploration zone in the 13y deposit (Fig. 2) to determine the Ra-bearing mineral phases. These samples, with an SPPγ activity between 160 and 530 c/s, are from reduced fine- to medium-grained gray sands with variable micaceous and organic matter contents.

b. HRpGS determinations of ^{226}Ra, ^{230}Th and ^{238}U

Uranium contents and Ra/U disequilibria were measured using a Canberra Falcon 5000 gamma spectrometer, installed at the GeoRessources laboratory and optimized for the measurements of samples of constant sampling volume and well isolated from the environment. The spectrometer consisted of an electrically cooled broad energy high purity germanium (HPGe) detector, calibrated with standard radioactive sources by Canberra. A 50 mm thick lead brick shield was designed to lower the background radiation, and a 2-mm thick folded copper sheet was used to further shelter the sample and the detector from the Pb X-rays. The background dose rates were thus reduced by a factor >2 by our shielding device, with rates <0.15 µSv/h within the Pb enclosure.

Background spectra were acquired for 62-113 hours over the measurement period (10/2013 - 07/2014), with fairly constant levels. They were dominated by the ^{40}K (1460 keV) and ^{214}Bi photopeaks (609, 1764 keV), very weak peaks were detected for some of the daughter nuclides of the U decay chains: including ^{234m}Pa (<200 counts per day) and ^{235}U-^{226}Ra (<1500 counts per day). The background photopeak areas were subtracted from the samples.

Sample aliquots were placed directly in contact with the detector, protected by a polyethylene film in cylindrical supports, 95 mm in diameter, after eventual gross disaggregation of the cohesive samples. Acquisitions were performed for 3-138h, depending on the sample mass and U content.

Laboratory γ spectrometry ^{238}U quantitative assays often rely on the low energy emissions (at 63.3, 92.4 and 92.8 keV) during β decay of the ^{234}Th (Déjeant et al., 2014), which are however rapidly absorbed by the sample (within a few millimeters). Our approach favored the geologic representativity of assays, using the less probable but higher energy 1001 keV photopeak associated with ^{234m}Pa, with a higher penetrative power. Such a strategy also benefits from the efficacy of detection being independent from sample mineralogy at such high energies.

The U and Ra contents were thus derived from the net areas of the 186 and 1001 keV photopeaks and from the counting efficiency of the detector at these energies, provided by the ISOCS (In Situ Object Calibration Software) code (Venkataraman et al., 1999). The experimental settings were modeled with the “simple cylinder” template, which was set up with the geometry and characteristics of the samples (thickness, density, chemical composition).

Uranium activity was directly derived from the net area of the 1001 keV photopeak. The interferences and peak sum corrections were always less than 5‰, i.e., at least an order of magnitude lower than the error in the U activity determinations. The energy resolution of the Falcon 5000 at the 186.2 keV photopeak of ^{226}Ra is insufficient to directly resolve the interference with the ^{235}U photopeak (185.7 keV). We assessed the area of the interfering ^{235}U photopeak using the natural relative abundance of the U isotopes ($\mathcal{R}$ = ^{238}U/^{235}U = 137.794 ± 0.027; Goldmann et al., 2015), considering that the potential ^{238}U/^{235}U fractionation is much less than the error in the counting efficiency of the detector (usually > 6%), which usually contributes most to the error. This is supported in the recent studies by Uvarova et al. (2014) and Placzeck et al. (2016), in which the reported δ^{238}U in U ores never exceeds 5‰.

The ^{235}U activity is derived as:

$$^{235}U = \frac{^{238}U \times \mathcal{M}_{^{238}U} \times \tau_{^{238}U}}{\mathcal{R} \times \mathcal{M}_{^{235}U} \times \tau_{^{235}U}} \quad \text{(eq. 1)}$$

with $\mathcal{M}_{^{238}U}$, the molar weight of ^{238}U;

$\mathcal{M}_{^{235}U}$, the molar weight of ^{235}U;

$\tau_{^{238}U}$, the half-life of ^{238}U;

$\tau_{^{235}U}$, the half-life of ^{235}U;

The ^{226}Ra activity is then obtained by correcting the Ra activity derived from the total 186 keV photopeak ($Ra_{186\,tot}$) as:

$$Ra = Ra_{186\,tot} - ^{235}U \times \frac{br_{^{235}U_{186keV}}}{br_{^{226}Ra_{186keV}}} \quad \text{(eq. 2)}$$

where $br_{^{235}U_{186keV}}$ is the branching ratio of ^{235}U at 185.7 keV and $br_{^{226}Ra_{186keV}}$, the branching ratio of ^{226}Ra at 186.2 keV.

The activity of ^{230}Th is derived from the 67.67 keV photopeak area.

The photopeak intensities, nuclide half-lives and branching ratios were extracted from the JEFF-3.1.1 library (OECD/NEA Data Bank, 2009).

Eleven sample powders with U contents in the range 0-17000 ppm, analyzed by ICP-MS at Areva's SEPA laboratory, were measured using our system. The results are presented in Table 2 and Figure 3. Our U contents are perfectly correlated (R^2 = 0.99995) with the previous ICP-MS determinations, defining a linear trend computed using the linear regression tool in Isoplot (Ludwig, 1992), as y = 0.97 (±0.03) x + 2.7 (±4.1).

c. Characterization of the main U microsites

Optical and scanning electron microscopy (SEM) in back-scattered electron mode (BSE) were used to characterize the textures and the mineralogical relationships between pyrite, U-bearing minerals and Fe-Ti-oxides. SEM images were obtained using BSE mode to reveal the elemental zoning and changes in the mean atomic number (Z), using a JEOL J7600F SEM equipped with a silicon drift detector type energy-dispersive spectrometer (EDS) and an Oxford Wave wavelength-dispersive spectrometer (WDS).

Electron microprobe analyses (EMPA) were performed at SCMEM-GeoRessources on a CAMECA SX100 instrument equipped with a wavelength dispersive spectrometer (WDS), calibrated using natural and synthetic oxides (albite (Si), Al_2O_3 (Al), andradite (Ca), $BaSO_4$ (S, Ba), hematite (Fe), $MnTiO_3$ (Mn, Ti), olivine (Mg), orthoclase (K), $SrSO_4$ (Sr), UO_2 (U)). Total Fe is presented as FeO. Structural formulas were calculated on the basis of 3 oxygens for ilmenite, 9 for pseudo-rutile and 2 for the TiO_2 polymorphs.

Local Ra/U disequilibrium measurements have been conducted on very well studied ilmenite sections (previously investigated with SEM, EMPA, LA-ICP-MS and Raman). Uranium and Ra were determined using the secondary ion mass spectrometry (SIMS) microprobe CAMECA IMS-1270 at CRPG-CNRS (Vandoeuvre-lès-Nancy), according to the experimental protocol described by Deloule et al. (2002). The primary O^- ion beam was accelerated at 13 kV, with a primary current intensity varying between 10 and 25 nA. The size of the analysis spot was 25 µm. The mass and energy calibrations were checked before each measurement, after a 2 min pre-sputtering. To define the relative sensitivity factor for Ra and U used for samples, the empirical linear relationship of Compston et al. (1984) was defined on a Zambian uraninite as reference material.

4. Results

a. Distribution of ^{226}Ra and ^{238}U in the samples

Mineral separations (granulometry and magnetic sorting) were performed on the five representative high Ra/U sandstones from the 13y deposit (Fig. 2), to measure and document the relative distribution of U and Ra within the samples. Each separated fraction was counted by HRpGS (Table 3).

The finest mineral fractions separated (<63 µm) usually make up less than 5% of the total mass of the samples, except in sample 2871, where they reach almost 11%. These fractions reflect the overall mineral composition of the bulk samples. They are indeed quartz and feldspar dominated but in addition contain grains of ilmenite, monazite, zircon, and euhedral and framboidal pyrites. As confirmed by X-ray diffractograms and SEM observations, small amounts of smectite sometimes marginally cover detrital grains, typically supporting coffinite grains. The finest fractions are enriched throughout in U and Ra with respect to the bulk sample, both by factors ranging from 2- to 5-fold (Table 3, Fig. 4), implying contrasting Ra/U ratios. Two of these are less than 2 times larger than the bulk rock Ra/U ratio, while the others are as much as 5 times smaller.

The fractions of sample 3240 contribute crucial information about the relative distribution of U and Ra. Every paramagnetic fraction, whatever its granulometry, carries up to 1 order of magnitude more Ra than its amagnetic equivalent (Table 3, Fig. 5). The role of the magnetic mineral phases in carrying Ra is further highlighted by their relative weight with respect to the bulk sample, since magnetic fractions constituting only 5.5 % of the total weight contribute 21% of the total Ra activity in sample 3240 (Fig. 5). The smaller granulometric fractions (<160 µm) present the highest U and Ra activities, showing that the mineral phases carrying them are rather small and most probably contribute to the U-Ra concentrations in coarser (quartz-feldspar) fractions, as mixed grains. Within the small granulometric fraction ($63 < Ø < 160$ µm), the magnetic separate showed the highest U and Ra activities and has about a 4-5 times higher concentration of these elements than any other magnetic separate. The sole $63 < Ø < 160$ µm magnetic separate, likely to be the purest concentrate of magnetic minerals, was less than 1 wt.% of the whole rock and accounts for 10% of the total Ra activity in the 3240 sample. This fraction is mostly constituted of ilmenite grains at various stages of alteration, covered by pyrite and carrying coffinite.

b. U and Ra (Ba) carriers

At the secular equilibrium, the Ra contents are 3.4×10^{-7} less than the U contents, which range from 500 to a few thousands of ppm. Such values are not measurable by most of the

standard micro-analytical techniques (e.g., EMPA, LA-ICP-MS), and are only accessible to the high sensitivity of ion source mass spectrometry techniques. Chemically, Ra behaves similarly to other divalent alkaline earth elements, especially to Ba (Langmuir and Riese, 1985); it can be frequently incorporated at trace level in Ba-rich phases. Preliminary research to identify the potential Ra carriers has thus been focused on the typically ~10^7 times more abundant Ba (Porcelli and Swarzenski, 2003), as a proxy for Ra presence. As Ra disequilibrium arises from either U lixiviation or Ra uptake, we especially targeted (1) newly formed Ba-carrying mineral phases and (2) altered U-carrying minerals.

To confidently identify the U and Ra carriers, minerals were characterized on bromoform separated subsets of the 63 < Ø < 160 µm and 160 < Ø < 400 µm granulometric fractions of a number of samples from the 600-PA profile and the 13y orebody.

i. *Newly formed Ba-rich minerals*: Rare subhedral barite sections ≥100 µm in size have been encountered in 2 out of the 15 analyzed samples of the 600-PA profile (A7 and N3, in the oxidized and reduced zones, respectively). These sections incorporate small amounts of Sr, Na and Al (see Supplementary Table S1), but U remained below the detection limit of EMPA (<4500 ppm) and was not detected in LA-ICP-MS experiments either. A few exploratory assays were conducted with the ion microprobe, but Ra also remained below detection limits. A few of the detrital K-feldspars present in the samples were analyzed by EMPA to determine the potential of their alterations as a local Ba source for the neoformed phases. As in the case of U in barites, Ba content in K-feldspars remained under the detection limit of EMPA (<3600 ppm). However, three LA-ICP-MS analyses detected 106 ± 25 to 925 ± 278 ppm of Ba (see Supplementary Table S2).

ii. Altered minerals carrying U: The magnetic properties of the Ra carriers highlighted in the previous section led us to study the Fe-Ti mineral clusters. Their role as traps for U in low temperature diagenetic conditions has recently been proposed by Lach et al. (2015) and Mathieu et al. (2015). We present here major elements EMP analyses of the Fe-Ti oxides, including Ba measurements. To describe the ilmenite grains altered to a varied extent to pseudo-rutile and even rutile, we will later refer to ilmenite sensu lato (s.l.). On the other hand, the mineralogical species ilmenite or the as yet unaltered ilmenite sections will later be referred to as ilmenite sensu stricto (s.s.).

Two hundred forty-one Ba contents and 117 Sr contents (Supplementary Table 3) have been measured in ilmenite s.l. – TiO_2 sections covering the whole spectrum of ilmenite s.s. degradation and replacement by TiO_2, previously described in detail (Pownceby, 2010). Ilmenites s.s. and slightly altered ilmenites (Ti/[Ti+Fe] < 0.65) generally do not incorporate significant amounts of Sr or Ba, the mean Ba content barely reaching the detection limit. On the other hand, the Ba content of pseudo-rutile ranges between 0.1 and 0.9%, with an average of 0.32% (σ=0.15). Strontium content reaches 0.26%, with an average of 0.06% (σ=0.05). The severe structural changes taking place in the ultimate stages of ilmenite s.l. alteration release the trace elements incorporated during the previous alteration phases (Pownceby, 2010).

Our new measurements thus support the progressive sorption of Ba (and Sr) in the pseudo-rutile (Fig. 6) during the alteration process of ilmenite s.s. to pseudo-rutile. Such an incorporation of trace elements has previously been described in various alteration environments (Frost et al., 1983; Pownceby 2010) and for various metals. This is however, to

our knowledge, the first description of the incorporation of heavy alkaline earth elements. Considering the similarity in chemical behavior between Ba and Ra, the significant incorporation of Ba is a strong clue to the possible role of pseudo-rutile as an Ra carrier.

Ra/U *in-situ* measurement by SIMS

To conclusively demonstrate the uptake of Ra by ilmenite and its alteration products, ilmenite s.l. grains representative of the whole range of ilmenite s.s. alteration processes were targeted with the SIMS instrument IMS 1270 at the CRPG laboratory (Vandoeuvre-lès-Nancy, France), together with a number of associated U mineral sections in samples of the 600-PA profile and the TSU-27 block. The results are presented in Tables 4 and 5. The Ra/U disequilibria measured in ilmenite s.l. grains range between 0.4 ± 0.03 and 40.5 ± 2.5. The lowest Ra/U values (<1) for ilmenite s.l. are from measurements in the vicinity of a UO_2 section precipitated in the pores of altered ilmenite (Fig. 7). An unaltered ilmenite s.s. section was targeted and yielded an Ra/U of 1.4 ± 0.9. Higher grades of ilmenite s.l. alteration result in higher Ra/U values (Supplementary Figure S1). The latter strongly contrast with the very low values measured in U minerals, which range between 0.14 ± 0.02 and 0.70 ± 0.02 (average: 0.54 ± 0.13, 1σ). Such low Ra/U values were reported in the case of uraninites from the Imouraren uranium deposit (Deloule and Brouand, 2014), and were interpreted in terms of Ra leaching by protracted fluid-rock interaction.

Complementary isotopic data were collected on the ilmenites from sample 9628-H8 (Table 5), consisting in isotopes ^{234}U and ^{238}U, and ^{230}Th. The $^{234}U/^{230}Th$, $^{238}U/^{230}Th$ and $^{226}Ra/^{230}Th$ ratios exceed the secular equilibrium, with average ratios of 10.3 (σ = 11), 3.1 (σ = 1.8) and 15.6 (σ = 7.7), respectively. Since Th is considered an immobile element, this is further strong evidence for U and Ra uptake by ilmenites s.l.

c. Distribution of the Ra/U disequilibrium in roll-front deposits

The Ra/U ratio and the Ra and U contents of forty bulk samples distributed along the 600-PA profile were measured using HRpGS. The counting times ranged between 3 and 138 h, depending on the sample mass (18 to 340 g) and U content (10 to 14020 ppm).

The results are presented in Table 6 and Figure 8, where the Ra/U ratio is shown as a function of the U content. This figure shows that high disequilibria mainly affect barren samples, while the mineralized samples present low Ra/U ratios. This is consistent with the SIMS measurements of the Ra/U disequilibrium in mineralization sections (Table 4), which reach a maximum of 0.7. It also suggests that the roll-front nose and limbs are more likely to be in slight Ra-favorable Ra/U disequilibrium compared to the mineralization at the redox front. The highest Ra/U ratios corresponded to oxidized upstream samples, but most of the other high Ra/U ratios are from downstream reduced samples in the close vicinity of the mineralization (Fig. 9). Four unaltered reduced sandstone samples have been analyzed and present U contents between 10 and 30 ppm and Ra/U ratios in equilibrium within the error bars.

d. Control of Ra disequilibrium by the distribution of ilmenite s.l.

We report the qualitative abundance of ilmenites in samples on the 600-PA profile (Fig. 9), together with U abundances, the Ra/U disequilibrium and chemical gradient responsible for disequilibrium, when identifiable using ^{230}Th data. In this profile, most of the high Ra/U ratios

appear closely associated with ilmenite-rich samples, the rest appearing near the oxidized zones in contact with the clay caps of the aquifer (U leaching).

The samples from boreholes H and I are especially good examples of the role of ilmenites s.l. in the development of Ra disequilibria. These drill holes cross-cut the reduction front, and seven mineralized samples (U content >100 ppm, ≤4900 ppm) have been extracted from ten core samples. However, unless the U-minerals exhibit strong U-favorable disequilibria, five of these mineralized samples carry whole-rock excess Ra instead, with Ra/U up to 2.0 ± 0.3. In particular, sample H8 exhibits an Ra/U = 1.4 ± 0.1 for a uranium content over 1000 ppm. At the sample scale, the latter is characterized by dark beds of heavy minerals (Supplementary Figure S2) which mainly consist of ilmenites s.l., some of which presented SIMS Ra/U up to 19.9 ± 0.5 (Table 5). Interestingly, located about 9 m deeper into the borehole and also containing ilmenite beds, sample H9 presents one of the highest U contents (4867 ppm) but an Ra/U ratio of 1, contrasting with the U excesses of the mineralization. We interpret this as resulting from the mixing of U excess in the U minerals and Ra excess components in the ilmenites s.l.

e. Mixing model

For these calculations, the U mineralization is considered homogeneous, with an Ra/U ratio of 0.5 (average of 15 SIMS measurements, Table 4). The variables used in this simple calculation consist of the whole-rock U content, ilmenite abundance in the sample, and composition (in U and Ra/U). From these, the U fraction of the mineralization is calculated by subtracting the U load of the ilmenites population (ilmenites abundance x U content) from the whole-rock U content. The “equivalent U” Ra content of the mineralization is then calculated using the Ra/U ratio of the mineralization. The total Ra (equivalent U) load of the sample includes the mineralization load plus the Ra carried by the ilmenite population (U content x Ra/U x ilmenite abundance). Uranium contents of 1 to 20000 ppm were used as entry parameters for each model and the calculated Ra/U are plotted in Figure 9.

Such simple calculations show that our whole dataset for the 600-PA profile is framed by models involving ilmenites s.l. with average U contents less than 1% and average Ra/U of 5 - 15, which are intrinsically consistent with the range of our measurements. The abundance of ilmenites required in these models is rather modest (less than 2%) but perfectly consistent with the qualitative estimates (less than 5%).

5. Discussion

Ra scavenging by ilmenites s.l.

The mineral data as well as the whole-rock and mineral-fraction U/Ra analyses show that the ilmenite alteration products are traps for the incorporation of alkaline earth elements in the pseudo-rutile, in the same way as described for other metal traces in a number of previous studies of rocks devoid of U and Ra (Pownceby, 2010). Ti oxide surfaces apparently present noticeable affinity for alkaline earth elements, especially for the heaviest of them, Ba and Ra. The latter is often incorporated at an order of magnitude in excess of the U equilibrium, with U contents higher than the percent level. The measured Ra contents spread over 3 orders of magnitude, depending on the extent of ilmenite alteration.

The incorporation mechanism of such traces could not be determined precisely. Similar adsorption of Ba, Sr, and Ra has already been observed for illites (Hidaka et al., 2007). However, the surface of the ilmenite s.l. grains inspected using SEM is perfectly homogeneous down to the hundreds of nanometers scale. This indicates that either such elements substitute for Fe and Ti in the lattice, as previously proposed for Mn, Mg or Cr (Pownceby, 2010), or are directly absorbed or precipitated in the nano-porosity (e.g., Frost et al., 1983). Such phases were not detected using bi-variate discriminant diagrams of trace elements or by Raman spectroscopy.

As previously described (Pownceby, 2010 and references therein), the progressive alteration of ilmenites in pseudo-rutile and leucoxene involves progressive oxidation of ferrous iron and hydrolysis of the ilmenite, leading to its transformation into an Fe-Ti oxyhydroxide solid solution.

The surfaces of ferric hydroxide grains act as complexants for a number of ions in aquifers (Ames et al., 1983; Jambor and Dutrizac, 1998; Antelo et al., 2015; Zhu et al., 2013) and Ra enrichment in Fe and Mn oxides has been reported (Ames et al., 1983; Kronfeld et al, 1991; Thiry and Van Hees, 2008). The sorption of Ra in the environment has even been proposed to be dominat by iron phases (Soyer, 1984; Gundersen et al., 1992; Jambor and Dutrizac, 1998; Gonneea et al., 2008; Sajih et al., 2014). Furthermore, the sorption reactions of alkaline earth elements on the surface of hydrous ferric oxides have been proved to be endothermic (Mishra and Tiwary, 1999), which is interpreted in favor of a spontaneous surface complexation process. The extent of such complexation is further favored by concentration and pH of the solution (Mishra and Tiwary, 1999), and has been described as an inhibitor of the conversion of ferrihydrite to goethite or hematite (Jambor and Dutrizac, 1998). The typical size of ferrihydrite nanoparticles is in the range 1-10 nm (Hochella et al., 2008), which is far below the spatial resolution of our SEM images.

Furthermore, the affinity and sorption potential of Ti-hydroxides for a number of cations have been known and even considered for U recovery from seawater for decades (e.g., Davies et al., 1964; Kelmers, 1980). Sasaki et al. (1983) described exceptional ion-exchange properties of a synthetic hydrous Ti-dioxide with alkaline earth elements, among others. Later studies allowed the sorption sites to be identified (Venkataramani, 1993) and ultimately found applications in the nuclear industry and research, where specific implementations include radium separation from aqueous solutions (Andersen et al., 2003; Song et al., 2017).

The precise sorption mechanism operating for the alteration products of ilmenites remains elusive to date. However, both Ti and Fe hydroxides occurring as degradation products on the surface of ilmenite s.s. are likely to scavenge Ra from solutions.

Processes involved in the rupture of equilibrium

U and Ra have strongly contrasting chemical behavior. The mobility of U mostly depends on its oxidation state; in contrast, Ra is intrinsically insensitive to redox (e.g., Szabo et al., 2012; Brown et al., 2016). As its parent nuclide (^{230}Th) is also immobile in fluids, Ra release into groundwater mainly depends on the dissolution/leaching of “old” (i.e., Ra bearing) U minerals (Deloule and Brouand, 2014), marginally assisted by radiation damage or alpha-recoil effect of ^{230}Th decay. The ultimate breakdown of Ra-rich Fe-Ti oxides during their final stages of alteration is also likely to contribute locally to the redistribution of Ra. Such contrasting

behavior of U and both ^{230}Th and ^{226}Ra in groundwater results in a primary fractionation point in the decay chain of ^{238}U.

In the upstream oxidized zone, U is thus oxidized to the soluble U(VI) (Chabaux et al., 2003) and transported downstream, while ^{230}Th and ^{226}Ra remain rather immobile in oxidizing conditions (Soyer, 1984), thus producing high whole-rock Ra/U ratios (Ryan & O'Beirne-Ryan, 2009). This is exemplified by our sample 9628-B8, close to the redox front of the 600-PA profile, which presented a low U content (within the margins of error, equivalent to those of unaffected downstream reduced sandstones), a low ^{238}U/^{230}Th, and a ^{230}Th/^{226}Ra ratio in secular equilibrium. Without any further perturbation, the ^{230}Th (and ^{226}Ra) disequilibrium with respect to U isotopes should persist for a few tens of thousands of years (< 5 τ_{230Th}).

The soluble U(VI) lixiviated out of the oxidized ore is immobilized at the redox front, where the U ore presents strong Ra/U disequilibria in favor of U, as seen in the samples 9628-A6 or 9628-J12 that present high U contents, low ^{234}U/^{230}Th, and ^{230}Th/^{226}Ra in equilibrium.

The Ra immobilization can proceed (1) either from its co-precipitation with Ba or Sr sulfates or carbonates (Ballini et al., 2017), providing they exceed the solubility limit, or (2) from its adsorption on clay minerals in low pH conditions (Robin et al., 2017) or on Fe-Ti oxy-hydroxides.

The almost systematic slightly Ra-favorable disequilibrium envelope identified downstream of the mineralized nose of the roll-front conflicts with the lixiviation process. Indeed, U is only mobile in oxidizing conditions. The samples affected by such Ra disequilibria present whole-rock Ra excesses with respect to ^{230}Th, indicating significant Ra uptake at the sample scale (e.g., 600-PA samples 9628-F9; 9628-H8; 9628-I7 – 9628-I11). At the grain scale, as exemplified by the SIMS results acquired on the ilmenites s.l. of sample 9628-H8 (Table 5), the degradation products of ilmenites bear significant U and Ra disequilibria with respect to ^{230}Th (activity ratios often >10), indicating U and Ra uptake. The extremely variable ^{234}U/^{238}U ratios (between 0.3 and 6, on average 1.8 ± 1.0) determined in situ in these ilmenite s.l. sections further indicate multiple episodes of U sorption (Denton et al., 2016) from ^{234}U enriched groundwater, spreading over a protracted time range.

6. Conclusion

The *in-situ* alteration of detritic Fe-Ti oxides during the downstream progression of the roll-front lead to the incorporation of a number of trace elements, especially the heaviest elements of the alkaline earth group. This has fundamental consequences on the radioactive decay chains of U and their state with respect to the secular equilibrium. It additionally provides considerable insight into the geological processes underway during roll-front progression and evolution.

A general concept of the depletion/enrichment of Ra *vs.* U follows this model:

1) in the oxidized upstream portion of the orebody, the U depletion produces an Ra-favorable disequilibrium,

2) U is transported towards the mineralized front and precipitates together with Ra in uraninite with a U-favorable disequilibrium,

3) a further dissolution of the uraninite already deposited occurs as a function of the roll-front progression, leading to a remobilization of U and Ra,

4) the redox provokes the immobilization of the U at the roll-front,

5) downstream, the Ra which is insensitive to redox is taken up by the altered Fe-Ti oxides in the nose and limbs of the roll-front, forming an Ra-favorable radioactive disequilibrium aureole or halo.

As shown by our calculations, such an uptake is likely to be achieved by very small amounts of ilmenites (less than 2%), which is consistent with the proportions of ilmenite detected within the samples from the 600-PA profile.

This overall distribution is important to consider in any reserve estimation, with strong implications for exploration, mining operations, and post-operation remediation. The methodology used in this work indicates that systematic measurements in standardized conditions may be optimized with portable spectrometers. Such methods are suitable to be implemented at mining operation sites and may therefore be used to test or confirm the validity of assumptions involved in reserve calculations.

Acknowledgments

Two anonymous reviewers are thanked for their comments. We are grateful to G. Jones for revising the English. This work was supported by Orano and CNRS. The authors are grateful for the valuable technical support and expertise of the technical staff the experimental station exploitation of raw materials and residual substances (STEVAL) at the GeoRessources laboratory. Analytical work carried out on GeoRessources and CRPG platforms benefitted from funding from Labex RESSOURCES21 (Investissements d'avenir: ANR-10-LABX-21-01). We thank A. Flammang for his help in the preparation and polishing of epoxy resin mounts. We are also indebted to G. Bessaques for the skillful conception of the Falcon 5k shelf, Cu shielding and measurement bowls. The valuable knowledge and assistance of S. Mathieu, O. Rouer and L. Salsi with the SEM and EMPA is a greatly appreciated.

References

Alexeiev, D. V., H. E. Cook, V. M. Buvtyshkin, and L. Y. Golub (2009), Structural evolution of the Ural-Tian Shan junction: A view from Karatau Ridge, South Kazakhstan, C. R. Geosci., 341, 287–297. doi:10.1016/j.crte.2008.12.004.

Ames, L.L., McGarrah, J.E., Walker, B.A., Salter, P.F., 1983. Uranium and Radium sorption on amourphous ferric oxyhydroxyde. Chemical Geology, 40, 135-148.

Andersen, T. C.; Black, R. A.; Blevis, I.; Boger, J.; Bonvin, E.; Chen, M.; Cleveland, B. T.; Dai, X.; Dalnoki-Veress, F.; Doucas, G.; Farine, J.; Fergani, H.; Fowler, M. M.; Hahn, R. L.; Hallman, E. D.; Hargrove, C. K.; Heron, H.; Hooper, E.; Howard, K. H.; Jagam, P.; Jelley, N. A.; Knox, A. B.; Lee, H. W.; Levine, I.; Locke, W.; Majerus, S.; McFarlane, K.; McGregor, G.; Miller, G. G.; Moorhead, M.; Noble, A. J.; Omori, M.; Rowley, J. K.; Shatkay, M.; Shewchuk, C.; Simpson, J. J.; Sinclair, D.; Tanner, N. W.; Taplin, R. K.; Trent, P. T.; Wang, J.-X.; Wilhelmy, J. B.; Yeh, M. 2003. A radium assay technique using hydrous titanium oxide adsorbent for the Sudbury neutrino observatory. Nuclear Instruments and Methods in Physics Research Section A., 501(2), 386-398. doi: 10.1016/S0168-9002(02)01925-3

503 Antelo, J., Arce, F., Fiol, S., 2015. Arsenate and phosphate adsorption on ferrihydrite
504 nanoparticles. Synergetic interaction with calcium ions. Chemical Geology, 410, 53-62.
505 Ballini, M., Nos, J., Phrommavanh, V., Descostes, M. 2017. U and ^{226}Ra mobility in the
506 uranium mill tailings of Bellezane (France). *Goldschmidt Abstracts*, **2017** 218
507 Bande, A., Sobel, E. R., Mikolaichuk, A., Schmidt, A., Stockli, D.F., 2017. Exhumation history
508 of the western Kyrgyz Tien Shan: Implications for intramontane basin formation. Tectonics,
509 36, 163–180, doi:10.1002/2016TC004284.
510 Boulesteix T., Cathelineau M., Lach P., Deloule E., Brouand M., Fiet N., Toubon H., 2015.
511 Ilmenites and their alteration products, sinkholes for uranium and alkali earth in roll-front
512 deposits after the example of South Tortkuduk (Kazakhstan), in: Andre-Mayer, A.S.,
513 Cathelineau, M., Muchez, P., Pirard, E., Sindern, S. (Eds.), Mineral Resources in a
514 Sustainable World. Presented at the 13th SGA Biennial Meeting on Mineral Resources in a
515 Sustainable World, pp. 1781–1784
516 Brown, S.T., Basu, A., Christensen, J.N., Reimus, P., Heikoop, J., Simmons, A.,
517 Woldegabriel, G., Maher, K., Weaver, K., Clay, J., DePaolo, D.J. 2016. Isotopic Evidence for
518 Reductive Immobilization of Uranium Across a Roll-Front Mineral Deposit. Environmental
519 Science Technology, 50(12), 6189-6198. doi: 10.1021/acs.est.6b00626
520 Chabaux, F., Riotte, J., Dequincey, O. 2003. U-Th-Ra fractionation during weathering and
521 river transport. Reviews in Mineralogy and Geochemistry, 52(1), 533-576.
522 Compston, W., Williams, I.S., Meyer, C. 1984. U-Pb geochronology of zircons from lunar
523 breccia 73217 using a sensitive high mass-resolution ion microprobe. Journal of Geophysical
524 Research: Solid Earth 89: 525-534.
525 Dahlkamp, F.J. 2009. “Kazakhstan.” In *Uranium Deposits of the World*, edited by Franz J.
526 Dahlkamp, 181–89. Springer Berlin Heidelberg. doi:10.1007/978-3-540-78558-3_6.
527 Davies, R.V., Kennedy, J., McIlroy, R.W., Spence, R., Hill, K.M. 1964. Extraction of uranium
528 from Sea Water. Nature 203 (4950): 1110-1115. doi: 10.1038/2031110a0.
529 Déjeant, A., Bourva, L. Sia, R., Galoisy, L., Calas, G., Phrommavanh, V., Descostes, M.,
530 2014. Field analyses of ^{238}U and ^{226}Ra in two uranium mill tailings piles from Niger using
531 portable HPGe detector. Journal of Environmental Radioactivity, 137, 105-112.
532 Deloule, E., Alexandrov, P., Cheilletz, A., Laumonier, P., & Barbey, P. (2002). In-situ U-Pb
533 zircon ages for Early Ordovician magmatism in the eastern Pyrenees, France: the Canigou
534 orthogneisses. International Journal of Earth Sciences, 91(3): 398–405.
535 Deloule, E. and Brouand, M. 2014. Effect of Radium mobility on the U-Pb systematic and age
536 determination of uraninite. Geophysical Research Abstracts, Vol.16-EGU2014-9506, Vienna
537 (Austria).
538 Denton, J.S., Goldstein, S.J., Paviet, P., Nunn, A.J., Amato, R.S., Hinrichs, K.A., 2016. A
539 record of uranium-series transport at Nopal I, Sierra Peña Blanca, Mexico: Implications for
540 natural uranium deposits and radioactive waste repositories. Chemical Geology ,434, 12-27.
541 Frost, M.T., Grey, I.E., Harrowfield, I.R., Mason, K. 1983. The dependence of alumina and
542 silica contents on the extend of alteration of weathered ilmenites from Western Australia.
543 Mineralogical Magazine, 47: 201-208.
544 Goldmann A., Brennecka G., Noordmann J., Weyer S., Wadhwa M., 2015. The uranium
545 isotopic composition of the Earth and the Solar System. Geochimica et Cosmochimica Acta
546 148: 145–158.
547 Gonneea, M.E., Morris, P.J., Dulaiova, H., Charette, M.A., 2008. New perspectives on
548 radium behavior within a subterranean estuary. Marine Chemistry, 109, 250-267.
549 Gundersen, L.C.S., Schumann, R.R., Otton, J.K., Dubiel, R.F., Owen, D.E. Dickinson, K.A.
550 1992. The geology of Radon in the United States. in Gates, A. E., and Gundersen, L.C.S.,

eds., Geologic Controls on Radon: Boulder, Colorado, Geological Society of America Special Paper 271.
Hebert, B., Beaufort, D., Roy, R., Pouradier, A., Jikibayev, R. 2015. New Methods to Quantify Clay Minerals in the Uranium Deposits Hosted in Sands of the Chu Sarysu Basin (South Kazakhstan) Based on Visible and Near-Infrared Field Spectrometry. in: Andre-Mayer, A.S., Cathelineau, M., Muchez, P., Pirard, E., Sindern, S. (Eds.), Mineral Resources in a Sustainable World. Presented at the 13th SGA Biennial Meeting on Mineral Resources in a Sustainable World, pp 587-589.
Hébert, B., Baron, F., Robin, V., Lelievre, K., Dacheux, N., Szenknect, S., Mesbah, A., Pouradier, A., Jikibayev, R., Roy, R., Beaufort, D. 2019. Quantification of coffinite (USiO4) in roll-front uranium deposits using visible to near infrared (Vis-NIR) portable field spectroscopy. Journal of Geochemical Exploration 199: 53-59.
Hidaka, H., Horie, K., Gauthier-Lafaye, F., 2007. Transport and selective uptake of radium into natural clay minerals. Earth and Planetary Science Letters, 264, 167-176.
Hochella, Jr., M.F., Lower, S.K., Maurice, P.A., Penn, R.L., Sahai, N., Sparks, D.L., Twining, B.S., 2008. Nanominerals, mineral nanoparticles, and Earth systems. Science, 319, 1631-1635.
Ingham, E.S., Cook, N.J., Cliff, J., Ciobanu C.L., Huddleston, A. 2014. A combined chemical, isotopic and microstructural study of pyrite from roll-front uranium deposits, Lake Eyre Basin, South Australia. Geochimica et Cosmochimica Acta 125: 440-465.
Jaireth, S., McKay, A., Lambert, I. 2008. Association of large sandstone uranium deposits with hydrocarbons. Geoscience Australia News 89.
Jambor, J.L. and Dutrizac, J., 1998. Occurrence and Constitution of Natural and Synthetic Ferrihydrite, a Widespread Iron Oxyhydroxide. Chemical Reviews, 98(7), 2549-2585.
Kelmers, A.D. 1981. Status of Technology for the Recovery of Uranium from Seawater. Separation Science and Technology 16(9):1019-1035. doi: 10.1080/01496398108057597.
Kronfeld, J., Ilani, S., Strull, A., 1991. Radium precipitation and extreme ^{238}U-series disequilibrium along the Dead Sea coast, Israel. Applied Geochemistry, 6, 335-361.
Lach, P., Cathelineau, M., Brouand, M., Fiet, N. 2015. In-situ isotopic and chemical study of pyrite from Chu-Sarysu (Kazakhstan) roll-front uranium deposit. Procedia Earth and Planetary Science 13: 207-210.
Langmuir, D., and Herman, J.S., 1980. The mobility of Th in natural waters at low temperatures. Geochimica and Cosmochimica Acta, 44, 1753-1766.
Langmuir, D., and Riese, A.C. 1985. The thermodynamic properties of radium. Geochimica et Cosmochimica Acta 49(7): 1593-1601. doi: 10.1016/0016-7037(85)90264-9.
Ludwig, R. K., 1992. ISOPLOT a plotting and regression program for radiogenic-isotope data, version 2.57. US Geological Survey, Open File Report, 40
Mathieu R., Deschamps Y., Selezneva V., Pouradier A., Brouand M., Deloule E., Boulesteix T., 2015. Key mineralogical characteristics of the new South Tortkuduk uranium roll-front deposits, Kazakhstan, in: Andre-Mayer, A.S., Cathelineau, M., Muchez, P., Pirard, E., Sindern, S. (Eds.), Mineral Resources in a Sustainable World. Presented at the 13th SGA Biennial Meeting on Mineral Resources in a Sustainable World, pp. 1781–1784.
Mercadier, J., Cuney, M., Lach, P., Boiron, M.-C., Bonhoure, J., Richard, A., Leisen, M., Kister, P. 2011. Origin of uranium deposits revealed by their rare earth element signature. Terra Nova 23(4): 264-269. doi: 10.1111/j.1365-3121.2011.01008.x.
Mikhailov VV & Petrov NN. 1998. Age of exogene uranium deposits in south and south-east Kazakhstan according to the lead-isotope study. Geology of Kazakhstan 2(354): 63–70.

598 Mishra, S. and Tiwari, D. 1999. Ion exchangers in radioactive waste management. Part XI.
599 Removal of barium and strontium ions from aqueous solutions by hydrous ferric oxide.
600 Applied Radiation and Isotopes, 51, 359-366.
601 Munara, A. 2012. Formation des gisements d'uranium de type roll : approche minéralogique
602 et géochimique du gisement uranifère de Muyunkum (Bassin de Chu-Sarysu, Kazakhstan).
603 PhD thesis. Université de Lorraine, Nancy. 327 pp.
604 OECD/NEA Data Bank, 2009. The JEFF-3.1.1 Nuclear Data Library, JEFF Report 22,
605 OECD/NEA Data Bank (2009)
606 Plackzek, C.J., Heikoop, J.M., House, B., Linhoff, B.S., Pelizza, M. 2016. Uranium isotope
607 composition of waters from South Texas uranium ore deposits. Chemical Geology 437. 44-
608 55.
609 Porcelli, D., and Swarzenski, P.W., 2003. The behavior of U- and Th-series nuclides in
610 groundwater. Reviews in Mineralogy and Geochemistry, 52(1), 317-361.
611 Pownceby, M.I., 2010. Alteration and associated impurity element enrichment in detrital
612 ilmenites from the Murray Basin, southeast Australia: a product of multistage alteration.
613 Australian Journal of Earth Sciences, 57, 243-258.
614 Rallakis, D., Michels, R., Brouand, M., Parize, O., Cathelineau, M. 2019. The Role of Organic
615 Matter on Uranium Precipitation in Zoovch Ovoo, Mongolia. Minerals 9: 310.
616 Robin, V., Tertre, E., Beaucaire, C., Regnault, O., Descostes, M., 2017. Experimental data
617 and assessment of predictive modeling for radium ion-exchange on beidellite, a swelling clay
618 mineral with a tetrahedral charge. Applied Geochemistry 85, 1-9.
619 Ryan, R.J., O'Beirne-Ryan, A.-M., 2009. Uranium occurrences in the Horton Group of the
620 Windsor area, Nova Scotia and the environmental implications for the Maritimes Basin.
621 Atlantic Geology 45: 20pp. doi: 104138/atlgeol.2009.008.
622 Sajih, M., Bryan, N.D., Livens, F.R., Vaughan, D.J., Descostes, M., Phrommavanh, V., Nos,
623 J., Morris, K., 2014. Adsorption of radium and barium on goethite and ferrihydrite: A kinetic
624 and surface complexation modelling study. Geochimica et Cosmochimica Acta, 146, 150-
625 163.
626 Sasaki, T., Komatsu, Y., Fujiki, Y. 1983. Ion-exchange properties of hydrous titanium dioxide
627 with a fibrous form obtained from potassium dititanate. Solvent Extraction and Ion Exchange
628 1(4): 775-790, doi: 10.1080/07366298308918428
629 Song, L., Yang, Y., Luo, M., Dai, X. 2017. Rapid determination of radium-224/226 in
630 seawater by alpha spectrometry. Journal of Environmental Radioactivity 171:169-175. doi:
631 10.1016/j.jenvrad.2017.01.024
632 Soyer B. (1984) Geochemistry of uranium in the hydrographic network. In: De Vivo B.,
633 Ippolito F., Capaldi G., Simpson P.R. (eds) Uranium geochemistry, mineralogy, geology,
634 exploration and resources. Springer, Dordrecht.
635 Szabo, Z., DePaul, V.T., Fisher, J.M., Kraemer, T.F., Jacobsen, E. 2012. Occurrence and
636 geochemistry of radium in water from principal drinking-water aquifer systems of the United
637 States. Applied Geochemistry 27(3): 729-752. doi: 10.1016/j.apgeochem.2011.11.002.
638 Thiry, Y., and Van Hees, M. 2008. Evolution of pH, organic matter and ^{226}radium/calcium
639 partitioning in U-mining debris following revegetation with pine trees. Science of the total
640 environment, 393, 111-117.
641 Uvarova, Y.A., Kyser, T.K., Geagea, M.L., Chipley, D., 2014. Variations in the uranium
642 isotopic compositions of uranium ores from different types of uranium deposits. Geochimica
643 et Cosmochimica Acta, 146:1-17.
644 Venkataraman R, Bronson F, Abashkevich V, Young BM, Field M, 1999. Validation of in situ
645 object counting system (ISOCS) mathematical efficiency calibration software. Nuclear

Instruments and Methods in Physics Research Section A: Accelerators Spectrometers Detectors Associated Equipment. 422(1): 450-454.
Venkataramani, B., 1993. Characterization of sorption sites on hydrous titanium and thorium oxides by water sorption. Langmuir 9, 3026–3032. doi:10.1021/la00035a047
Zhu, M., Northrup, P. Shi, C., Billinge, S.J.L., Sparks, D.L., Waychunas, G.A., 2013. Structure of Sulfate Adsorption Complexes on Ferrihydrite. Environmental Science and Technology Letters, 2014, 1 (1), 97–101.

653 Figure captions

654 Figure 1: Maps localizing the Muyunkum uranium deposit in Kazakhstan (inset) and in the
655 local geologic context. The black rectangle in the inset stands for the extent of the main map.
656 The brownish overload on the main map corresponds to the Pre-Mesozoic basement. The
657 green and orange lines correspond to the regional scale redox fronts in the Upper
658 Cretaceous (dark green: middle; light green: upper) and Paleogene sands, respectively, as
659 drawn in Jaireth et al. (2008).

660 Figure 2: Map of the Tortkuduk mining licence in Southern Kazakhstan, displaying the
661 location of both sampling locations: the 13y and 17y orebodies. A detailed map of the 17y
662 orebody where the 600-PA profile (red line) has been cored is presented in the upper right
663 frame. The 600-PA geologic profile and the lithology of all the studied samples are presented
664 in the lower frame. The black vertical lines correspond to the drilling traces. Fm stands for
665 formation.

666 Figure 3: Correlation between the U concentrations measured by HRpGS and ICP-MS for a
667 selection of samples from Gabon, illustrating the accuracy of our γ-spectrometry approach.
668 The solid red line represents the weighted linear regression (see the end of section b in
669 Samples and Methods).

670 Figure 4: Relative U content and Ra/U between the bulk (filled symbols) and < 63 µm
671 fractions in the samples, illustrating the enrichment of the finest fractions in U and Ra with
672 respects to the bulk samples.

673 Figure 5: Global Ra repartition between the various mineral fractions within sample 3240.

674 Figure 6: Box and whiskers diagrams of the contents in alkaline earth elements (EMPA; Ca:
675 N = 394; Ba: N = 241; Sr: N = 117), illustrating their sorption during the alteration process of
676 ilmenite s.s. towards pseudo-rutile and its replacement by TiO_2. Red dashed lines
677 correspond to the theoretical Ti/(Ti+Fe) threshold between ilmenite s.s., pseudo-rutile and
678 the TiO_2 polymorphs. Dots represent the alkaline earth content averages of the Ti/(Ti+Fe)
679 subsets. Boxes correspond to the interquartile range. Black dashed lines reveal the range
680 between the lower and the higher fences. Red crosses represent the outliers to the content
681 population.

682 Figure 7: Section C17 across Fe-Ti clusters in the 600-PA profile 9628-H8 sample
683 investigated with the IMS1270 SIMS. Thin black circles represent the width of the ion beam,
684 the color code for their filling represents the intensity of Ra/U disequilibrium (lower part of the
685 figure). The red frames associated contain the U content and Ra/U value measured for each
686 targeted site (see the sketch in the lower part of the figure). White bold numbers correspond
687 to the analysis number in Table 5. Orange abbreviations correspond to: P-R: pseudo-rutile;
688 Pyr: pyrite; Ur: uraninite.

689 Figure 8: Ra/U ratio as a function of U content in samples from the 600-PA profile. The
690 colored lines stand for the impact of modeled abundance and composition of ilmenites s.l. on
691 the whole-rock Ra/U disequilibrium. The brown one corresponds to the model mixing 2% of
692 ilmenites with a U content of 1 wt.% and a Ra/U ratio of 15; the blue one corresponds to the
693 model mixing 0.5% of ilmenites with a U content of 1000 ppm and a Ra/U ratio of 5.

Figure 9: U content and Ra/U disequilibrium profile of the “600-PA” profile. Green zones correspond to the clay caps that frame the sandy aquifer. White and yellow colors respectively stand for the reduced and oxidized zones within the “Uyuk Fm.” (Dahlkamp, 2009) and the red pattern represents the mineralization. The “ilm” bubbles stand next to the samples in which ilmenites have been observed in thin sections; the yellow and orange colors are gradations for their qualitative abundance.

Table captions

Table 1: Overview of the samples recovered along the 600-PA profile, including their position within the roll-front and their redox state. The U and Ra contents measured using various methods are indicated, as well as the parameters for our gamma counting experiments.

Table 2: Results for the gamma countings of the selection of Gabon samples measured by ICP-MS. un. stands for uncertainty, D.L. stands for Detection Limit.

Table 3: U and Ra contents and Ra/U disequilibria measured by HRpGS on the bulk samples and mineral separates prepared from the high Ra/U disequilibrated samples.

Table 4: Results of the SIMS measurements of the Ra content and the Ra/U disequilibrium for both uraninite sections and their associated ilmenites s.l.

Table 5: Results of SIMS measurements on ilmenite s.l. sections of sample H8. The U content was retrieved by EMPA. Un. stands for uncertainty.

Table 6: Results of the gamma spectrometry measurements performed along the 600-PA profile. The ratios presented in the table are activity ratios. un. stands for uncertainty; n.d. for not determined.

716 Supplementary data:

717 Table S1: EMP analyses of baryte sections of the 600-PA profile. The numbers in italics
718 correspond to contents below the detection limit.

719 Table S2: Micro-analyses of K-feldspar sections. The Ba LA-ICP-MS measurements were
720 performed following the protocol described in Mercadier et al. (2011).

721 Table S3: EMP analyses of ilmenites, pseudo-rutiles and TiO_2 sections, sorted by ascending
722 Ti/(Ti+Fe).

723 Figure S1: SEM image of a pyrite-ilmenite s.l. cluster from the 13y orebody, examined with
724 the IMS 1270 ion probe. The ablation craters are marked by black dashed ellipses, within
725 which the measured Ra/U ratio is indicated in bold characters. Electron microprobe spots are
726 represented by colored dots, indexed on the Ti/(Ti+Fe) ratio in the structural formula. The
727 associated frames present the measured U and Ba contents (in percent).

728 Figure S2: Photographs and micro-photographs of the sample 9646-AF-5 particularly rich in
729 rather altered ilmenites (several percent), and other heavy minerals found in beds.

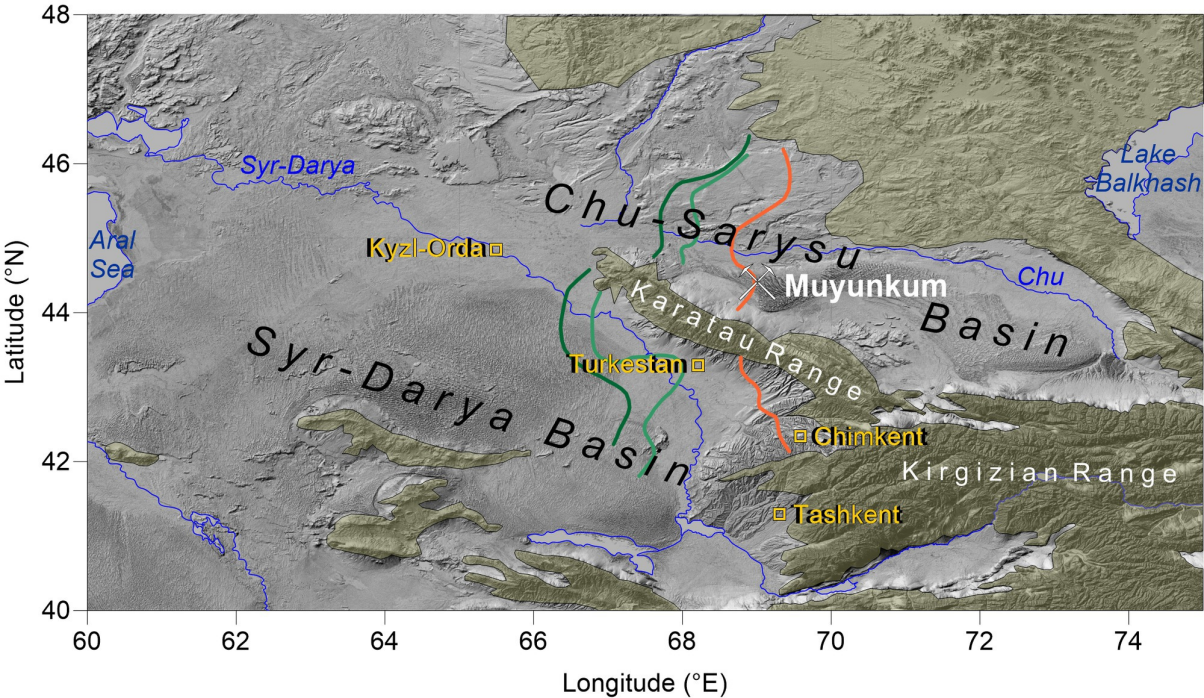
Syr-Darya
Aral Sea
Kyzl-Orda
Chu-Sarysu Basin
Karatau Range
Muyunkum
Chu
Lake Balkhash
Turkestan
Syr-Darya Basin
Chimkent
Kirgizian Range
Tashkent
Latitude (°N)
Longitude (°E)
48
46
44
42
40
60
62
64
66
68
70
72
74

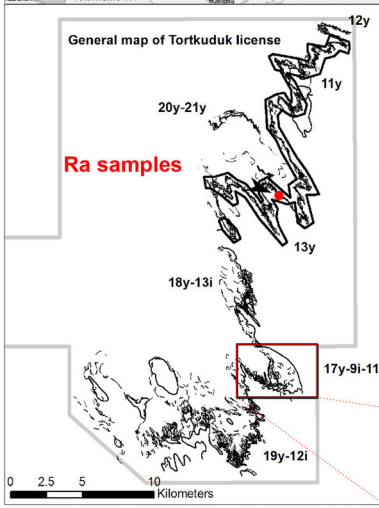

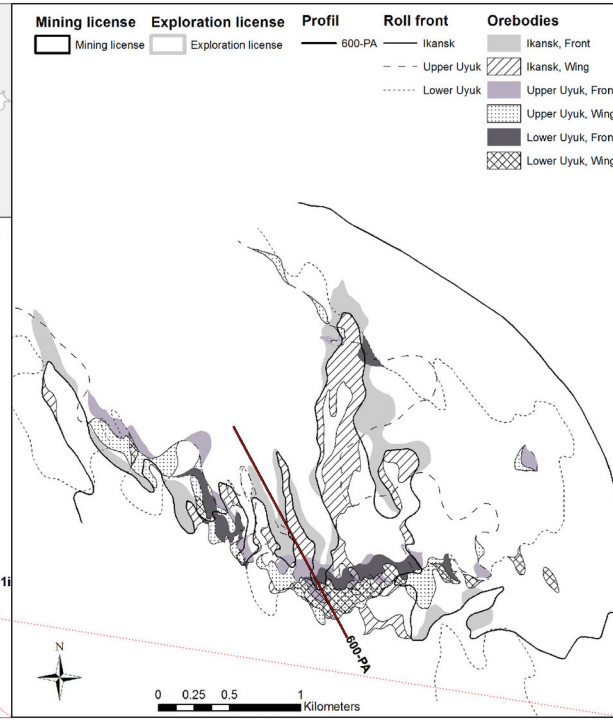

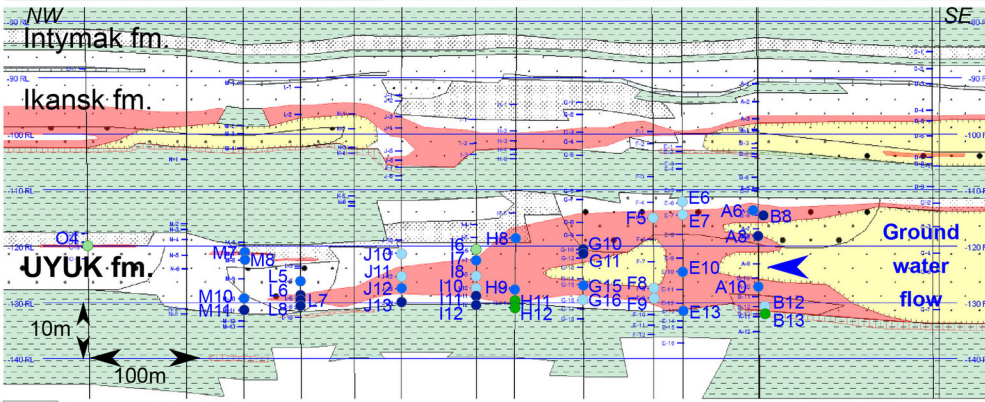

impermeable clay barriers

oxidized formations

redox front mineralization

reduced formations

- fine-grained sand
- medium-grained sand
- coarse sand
- clayey siltsone
- claystone

600-PA profile

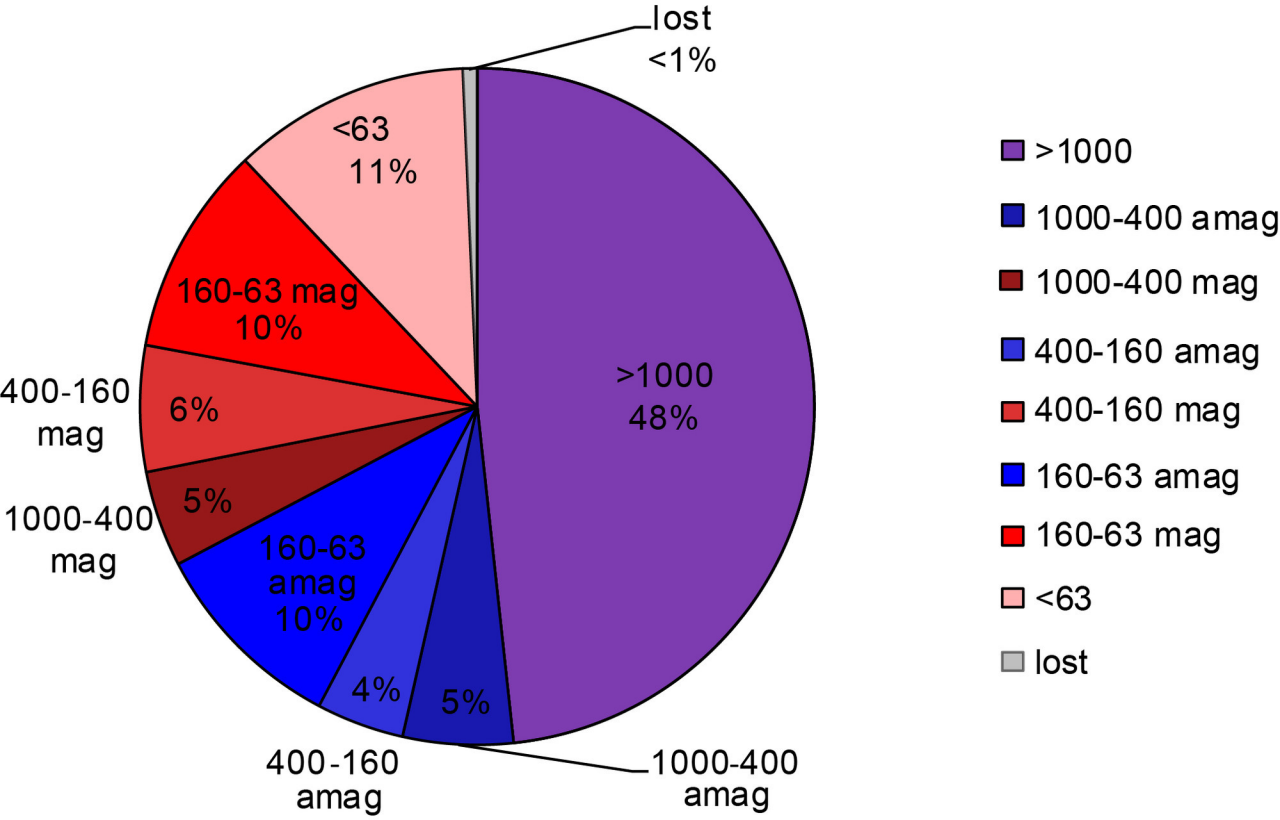
lost
<1%
<63
11%
160-63 mag
10%
400-160
mag
6%
1000-400
mag
5%
160-63
amag
10%
400-160
amag
4%
1000-400
amag
5%
>1000
48%
>1000
1000-400 amag
1000-400 mag
400-160 amag
400-160 mag
160-63 amag
160-63 mag
<63
lost

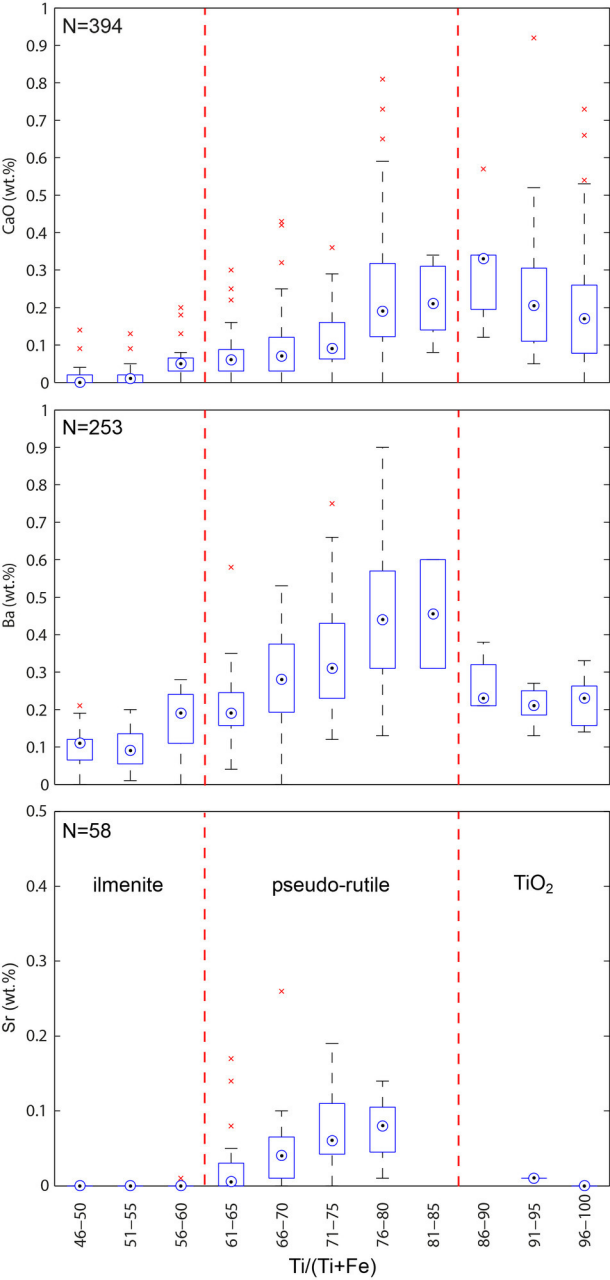
N=394
CaO (wt.%)
N=253
Ba (wt.%)
N=58
ilmenite
pseudo-rutile
TiO2
Sr (wt.%)
46–50
51–55
56–60
61–65
66–70
71–75
76–80
81–85
86–90
91–95
96–100
Ti/(Ti+Fe)

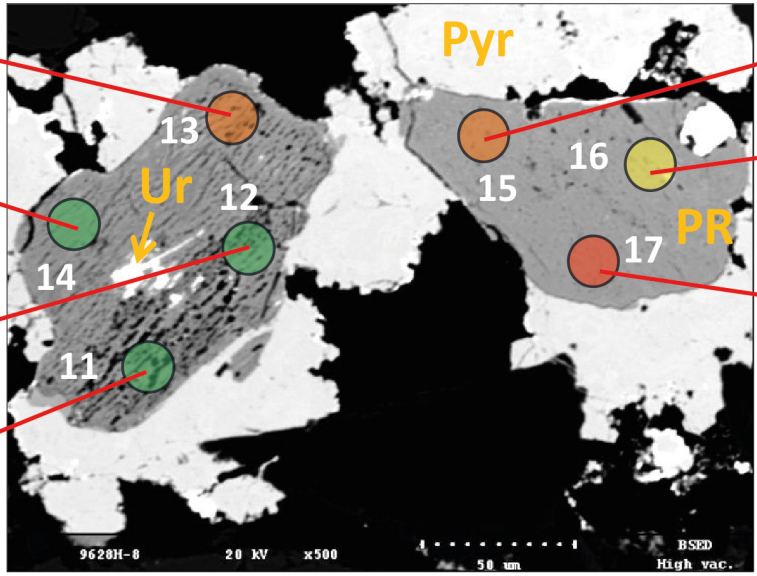

U (wt.%) EMP
Ra/U SIMS

Ra/U: <1.5 | 1.5-3 | 3-10 | >10

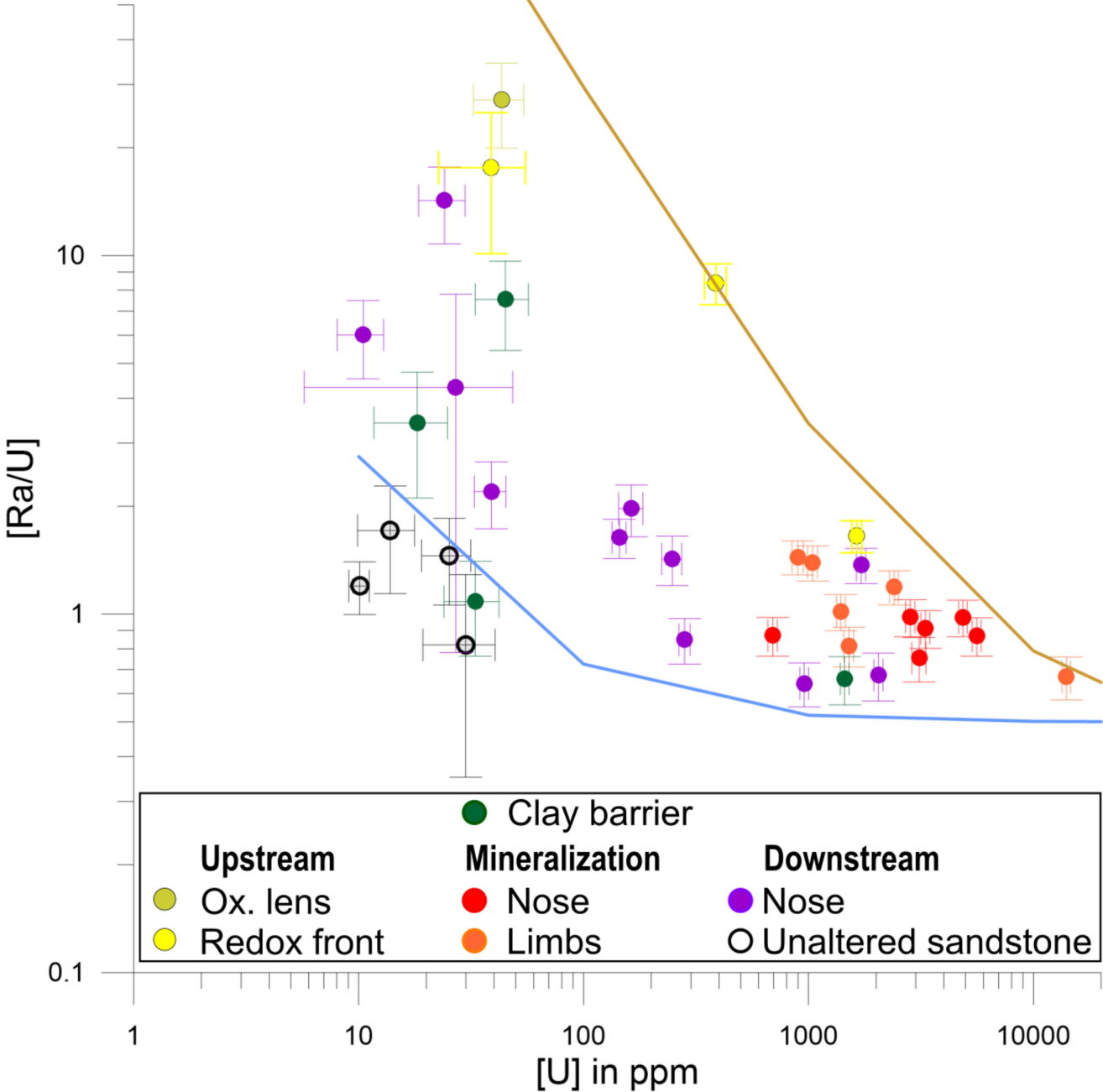
10
1
0.1
[Ra/U]
1
10
100
1000
10000
[U] in ppm
Clay barrier
Upstream
Ox. lens
Redox front
Mineralization
Nose
Limbs
Downstream
Nose
Unaltered sandstone

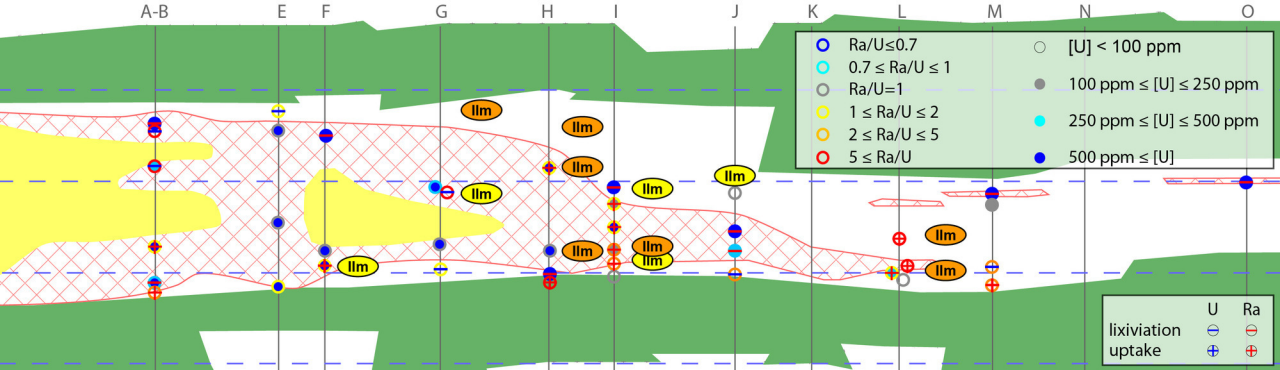
A-B
E
F
G
H
I
J
K
L
M
N
O
IIm
IIm
IIm
IIm
IIm
IIm
IIm
IIm
IIm
IIm
Ra/U≤0.7
0.7 ≤ Ra/U ≤ 1
Ra/U=1
1 ≤ Ra/U ≤ 2
2 ≤ Ra/U ≤ 5
5 ≤ Ra/U
[U] < 100 ppm
100 ppm ≤ [U] ≤ 250 ppm
250 ppm ≤ [U] ≤ 500 ppm
500 ppm ≤ [U]
U
Ra
lixiviation
uptake

N° 9628	position	Redox	SPPγ (c/s)	U-XRF (ppm)	U_ICP (ppm)	counted mass (g)	time (h)	[U] (ppm)	un.	[Ra] (ppt)	un.
A-6	*limb*	**R**	2500	7848	14290	34.9	9	14020	624	3164	410
A-8	*redox front*	**R**	420	335	340	87.3	5	388	43	1101	73
A-10	*redox front*	**R**	700	1552	1474	176	4	1641	82	915	81
B-8	*redox front*	**O**	160	35	18	30.5	73	39	16	231	15
B-12	*limb*	**R**	170	1475	1529	37	17	1513	76	416	49
B-13	*clay barrier*	**R**	120	71	20	70	62	18	7	20	2
E-6	*unaltered reduced sandstone*	**R**	100	10	n.d.	341	19	14	4	8	2
E-7	*limb*	**R**	400	1792	n.d.	343	14	1394	62	478	51
E-10	*mineralized front*	**R**	240	918	n.d.	164	4	694	34	204	23
E-13	*limb*	**R**	1200	3600	n.d.	534	4	2405	110	967	96
F-5	*mineralized front*	**R**	370	2055	n.d.	77.4	5	3106	219	790	97
F-8	*mineralized front*	**R**	650	4554	n.d.	164	3	2838	136	940	101
F-9	*limb*	**R**	450	2669	n.d.	224	3	897	51	436	41
G-10	*mineralized front*	**R**	840	3019	3319	175	4	5600	253	1644	187
G-11	*oxydized lens*	**O**	170	11	n.d.	64.5	62	43	11	391	24
G-15	*mineralized front*	**R**	350	3572	3864	53	13	3313	151	1020	114
G-16	*unaltered reduced sandstone*	**R**	100	22	21	65.1	35	25	6	12	1
H-8	*limb*	**R**	850	3484	3759	62.2	17	1043	53	490	49
H-9+10	*mineralized front*	**R**	1250	~4000	~5800	106	25	4867	211	1608	174
H11	*limb - clay barrier*	**R**	260	809	n.d.	243	13	1450	65	323	47
H-12	*limb - clay barrier*	**R**	160	38	35	35.9	105	45	12	113	8
I-6	*nose - reduced zone*	**R**	230	81	81	279	14	959	43	207	28
I-7	*nose - reduced zone*	**R**	360	97	84	194	15	144	10	80	8
I-8+9	*nose - reduced zone*	**R**	225	~2500	2122 (I8)	189	8	1714	79	793	78
I-10	*nose - reduced zone*	**R**	150	288	213	41.3	20	163	20	108	11
I-11	*nose - reduced zone*	**R**	110	33	38	194	34	39	6	29	4
I-12	*clay barrier*	**R**	100	27	23	43.5	120	33	9	12	1
J-11	*unaltered reduced sandstone*	**R**	90	n.d.	9	324	7	10	1	4	1
J-12	*nose - reduced zone*	**R**	230	1415	1174	173	6	2046	95	466	68
J-13	*nose - reduced zone*	**R**	140	524	465	293	8	282	16	81	11
J-14	*nose - reduced zone*	**R**	120	9	18	18.4	111	27	21	38	3
L-5	*nose - reduced zone*	**R**	100	9	n.d.	197	76	10	2	21	2
L-6	*nose - reduced zone*	**R**	140	13	18	204	39	24	6	116	7
L-7	*nose - reduced zone*	**R**	130	253	227	32.8	24	248	25	119	14
L8	*unaltered reduced sandstone*	**R**	90	15	13	74.7	19	30	11	8	4
M-7	*mineralization lens reduced zone*	**R**	400	4269	4566	25.6	17	4517	206	770	136
M-8	*mineralization lens reduced zone*	**R**	120	68	112	241	13	98	8	31	4
M10	*unaltered reduced sandstone*	**R**	120	23	27	54.1	138	30	7	35	3
M11	*unaltered reduced sandstone*	**R**	100	14	10	95.8	34	16	5	13	1
O-4	*mineralization lens reduced zone*	**R**	340	1285	1306	155	3	1384	72	354	50

Sample	Mass (g)	Counting time (h)	U_{ICP-MS} (ppm)	un. (ppm)	D.L. (ppm)	U_{HRpGS} (ppm)	un. (ppm)	Ra/U	un.
201210620001	77	4	0	-	65	*2*	*9*	*0.2*	*0.9*
201204836066	91	24	25	1	50	*23*	*6*	*1.2*	*0.3*
201210619030	215	21	50	3	34	*52*	*7*	*1.1*	*0.2*
201210625010	292	14	100	5	66	108	10	1.4	0.2
201210623021	180	21	508	25	100	523	27	1.1	0.1
201210628006	227	9	750	38	159	727	38	1.1	0.1
201210677008	204	4	1001	50	226	952	56	1.1	0.1
201210628026	217	3.3	1502	75	257	1489	79	1.1	0.1
201207521001	72	3.6	7507	375	609	7146	333	1.1	0.1
201207547042	99	3.5	9910	496	630	9401	429	0.9	0.1
201210628009	234	4.3	17575	879	951	16484	725	1.0	0.1

	Mineral separate		Counting parameters			[U] (ppm)			[Ra] (ppt)		$^{226}Ra/^{238}U$	
Sample	**Granulometry**	**Magnetism**	**mass (g)**	**duration (h)**	**ICP-MS**	**un.**	**HRpGS**	**un.**	**HRpGS**	**un.**	**HRpGS**	**un.**
2819-2	*bulk*		466	12	210	11	130	10	288	19	6.6	0.7
	Ø<63 µm		41	47			587	33	1151	79	5.8	0.5
2836	*bulk*		513	15	61	3	52	7	201	13	11.5	1.8
	Ø<63 µm		26	50			134	26	936	59	20.7	4.2
2868	*bulk*		510	17	13	1	13	7	283	17	63	35
	Ø<63 µm		25	34			193	33	769	50	11.8	2.1
2871	*bulk*		551	19	127	6	113	9	318	21	8.4	0.9
	Ø<63 µm		72	49			230	18	1242	75	16	1.6
3240	*bulk*		488	112	32	3	25	3	141	9	16	2.0
	Ø>1mm		277	25			45	6	214	14	14	2.0
	400< Ø <1000µm	*amagnetic*	213	118			9	2	30	2	10	2.0
	400< Ø <1000µm	*paramagnetic*	21	72			88	20	268	18	9	2.1
	160< Ø <400µm	*amagnetic*	176	34			9	3	29	2	10	3.6
	160< Ø <400µm	*paramagnetic*	13	19			29	16	404	25	41	22
	63< Ø <160µm	*amagnetic*	91	47			20	7	129	8	19	6.2
	63< Ø <160µm	*paramagnetic*	6	49			207	80	1502	95	21	8.4
	Ø<63 µm		33	62			117	17	427	28	11	1.7

	Ra (ppb)	Ra/U	un.
UO2			
9578_126B_U@1	189	0.63	0.03
9578_126B_U@2	198	0.66	0.02
9578_126B_U@3	210	0.70	0.02
9578_126B_U@4	208	0.70	0.02
9578_126B_U@6	180	0.60	0.02
9578_126B_U@7	211	0.70	0.02
9578_126B_U@8	167	0.56	0.01
9578_126B_U@10	89	0.30	0.05
9578_126B_U@11	104	0.35	0.05
9578_126B_U@12	122	0.41	0.06
9578_126B_U@12	182	0.61	0.02
9578_126B_U@13	193	0.65	0.01
9578_126B_U@14	176	0.59	0.02
9578_126B_U@15	172	0.58	0.02
9578_126B_U@15	41	0.14	0.02
Ilmenites			
9578_126B_il@1	29	38	16
9578_126B_il@2	89	23	0.7
9578_126B_il@5	86	16	0.4
9578_126B_il@6	64	14	0.6
9578_126B_il@7	127	21	1.3
2871-C3@1	60	30	1
2871-C3@3	3	30	4
2871-C3@4	13	28	5
2871-C3b@1	77	23	1
2871C3b@2	117	28	2
2871-C3b@3	53	37	3
2871-C3b@4	103	22	1
2871-C3b@5	66	23	1
2871-C3b@6	74	20	1
2871-C3b@8	2	28	2
2871-C3b@9	5	26	2
2871-C3b@10	45	23	2
2871-C3c@1	111	34	3
2871-C3c@2	99	29	2
2871-C3c@1	111	34	3
2871-C3c@3	95	34	3
2871-C3c@4	84	23	2
2871-C3c@5	62	23	1
2871-C3c@6	52	40	3
2871-C3c@7	20	26	2

	U (wt.%)	$[^{234}U/^{238}U]$	un.	$[^{230}Th/^{238}U]$	un.	$[^{226}Ra/^{238}U]$	un.
H8-13@1	0.93	0.81	0.03	0.59	0.07	19.9	1.3
H8-13@2	1.01	0.90	0.03	0.71	0.07	16.4	1.0
H8-13@3	1.24	6.0	0.9	0.60	0.05	8.1	0.9
H8-13@4	0.37	0.75	0.07	0.38	0.06	6.9	2.5
H8-14@1	0.53	1.17	0.10	0.83	0.06	8.8	0.9
H8-14@2	1.15	2.12	0.12	0.22	0.02	7.3	0.7
H8-14@3	0.59	0.90	0.06	0.66	0.06	9.3	1.2
H8-14@8	1.3	1.81	0.05	0.18	0.01	4.4	0.5
H8-14@9	0.83	0.68	0.02	0.46	0.03	14	1
H8-14@10	0.63	0.67	0.03	0.59	0.04	9.2	0.8
H8-17@11	2.74	4.0	0.6	0.22	0.01	1.1	0.1
H8-17@13	1.24	1.7	0.1	0.25	0.02	5.9	0.4
H8-17@14	5.39	0.42	0.01	0.21	0.01	0.42	0.03
H8-17@15	0.58	0.84	0.05	0.26	0.02	9.1	0.7
H8-17@16	1.67	2.7	0.1	0.11	0.004	2.7	0.2
H8-17@17	0.62	0.55	0.01	0.43	0.04	12.7	0.7
H8-16@18	1.53	2.0	0.1	0.55	0.02	5.5	0.4
H8-16@19	2.23	1.7	0.1	0.53	0.01	6.9	0.4
H8-16@20	1.25	2.0	0.1	0.44	0.01	7.0	0.2
H8-16@22	1.72	2.4	0.1	0.53	0.03	6.5	0.5
H8-16@23	2.1	0.46	0.01	0.54	0.02	1.9	0.2
H8-11@24	0.42	1.6	0.1	0.63	0.06	3.5	0.4
H8-11@25	1.06	1.7	0.1	0.93	0.03	2.4	0.2
H8-11@26	1.17	1.6	0.05	0.47	0.02	4.1	0.2
H8-10@27	0.27	2.7	0.2	0.66	0.05	2.2	0.5
H8-10@28	0.25	3.2	0.2	0.33	0.03	4.1	1.2
H8-10@29	0.27	2.8	0.2	0.85	0.08	4.5	0.5
H8-10@30	0.12	0.31	0.03	1.11	0.16	18	3
H8-10@31	0.07	0.8	0.1	0.05	0.02	1.4	0.9
H8-10@32	0.38	0.67	0.04	0.61	0.07	4.9	0.8
H8-10@33	0.13	0.68	0.05	0.80	0.17	9.7	1.9
H8-25@34	1.84	0.98	0.03	0.43	0.02	8.0	0.3
H8-25@35	1.41	3.5	0.2	0.29	0.01	4.5	0.3
H8-25@36	2.37	3.2	0.2	0.30	0.01	6.0	0.4
H8-25@37	1.87	3.4	0.2	0.30	0.02	4.1	0.3

Sample	Mass (g)	Counting time (h)	U_{ICP-MS} (ppm)	un. (ppm)	D.L. (ppm)	U_{HRpGS} (ppm)	un. (ppm)	Ra/U	un.
201210620001	77	4	0	1	65	*2*	*9*	*0.2*	*0.9*
201204836066	91	24	25	1	50	*23*	*6*	*1.2*	*0.3*
201210619030	215	21	50	3	34	*52*	*7*	*1.1*	*0.2*
201210625010	292	14	100	5	66	108	10	1.4	0.2
201210623021	180	21	508	25	100	523	27	1.1	0.1
201210628006	227	9	750	38	159	727	38	1.1	0.1
201210677008	204	4	1001	50	226	952	56	1.1	0.1
201210628026	217	3.3	1502	75	257	1489	79	1.1	0.1
201207521001	72	3.6	7507	375	609	7146	333	1.1	0.1
201207547042	99	3.5	9910	496	630	9401	429	0.9	0.1
201210628009	234	4.3	17575	879	951	16484	725	1.0	0.1

Slope = 0.969±0.051 (2σ)
Inter = 2.7±8.1
Xbar = 50.5073, Ybar =51.5934

		Analytic conditions		
Element	Standard	Acc. voltage	Current	Counting time
Al	Al_2O_3	15 kV	12-20 nA	10 s
Ba	$BaSO_4$	15-20 kV	20-150 nA	30-60 s
Ca	andradite	15-20 kV	12-100 nA	10-20 s
Fe	Fe_2O_3	15 kV	12-20 nA	10 s
K	orthose	15 kV	12-20 nA	10 s
Mg	olivine	15-20 kV	12-100 nA	10-20 s
Mn	$MnTiO_3$	15 kV	12-20 nA	10 s
S	$BaSO_4$	15 kV	150 nA	40 s
Si	albite	15 kV	12-20 nA	10 s
Sr	$SrSO_4$	15 kV	20-150 nA	30-40 s
Ti	$MnTiO_3$	15 kV	12-20 nA	10 s
U	UO_2	15-20 kV	20-150 nA	20-60 s

	Mineral separate		Counting parameters			[U] (ppm)			[Ra] (ppt)		$^{226}Ra/^{238}U$	
Sample	**Granulometry**	**Magnetism**	**mass (g)**	**duration (h)**	**ICP-MS**	**un.**	**HRpGS**	**un.**	**HRpGS**	**un.**	**HRpGS**	**un.**
2819-2	*bulk*		466	12	210	11	130	10	288	19	6.6	0.7
	Ø<63 µm		41	47			587	33	1151	79	5.8	0.5
2836	*bulk*		513	15	61	3	52	7	201	13	11.5	1.8
	Ø<63 µm		26	50			134	26	936	59	20.7	4.2
2868	*bulk*		510	17	13	1	13	7	283	17	63	35
	Ø<63 µm		25	34			193	33	769	50	11.8	2.1
2871	*bulk*		551	19	127	6	113	9	318	21	8.4	0.9
	Ø<63 µm		72	49			230	18	1242	75	16	1.6
3240	*bulk*		488	112	32	3	25	3	141	9	16	2.0
	Ø>1mm		277	25			45	6	214	14	14	2.0
	400< Ø <1000µm	*amagnetic*	213	118			9	2	30	2	10	2.0
	400< Ø <1000µm	*paramagnetic*	21	72			88	20	268	18	9	2.1
	160< Ø <400µm	*amagnetic*	176	34			9	3	29	2	10	3.6
	160< Ø <400µm	*paramagnetic*	13	19			29	16	404	25	41	22
	63< Ø <160µm	*amagnetic*	91	47			20	7	129	8	19	6.2
	63< Ø <160µm	*paramagnetic*	6	49			207	80	1502	95	21	8.4
	Ø<63 µm		33	62			117	17	427	28	11	1.7

	SiO_2	Al_2O_3	FeO	Na_2O	K_2O	Ba	Total	Ba (ppm)	Sr (ppm)
d.l. (wt.%)	0.11	0.08	0.22	0.08	0.06	0.36		LA-ICP-MS	
std.dev	2%	2%	42%	25%	3%	/			
M8-c2	63.9	18.1	0.46	0.27	16.3	0	99.08	164	17
M8-c6	64.6	18.6	0.83	0.56	15.7	0.1	100.43		
M8-c11c	65.0	18.2	*0.1*	0.66	16.2	0.1	100.27	255	206
M8-c11r	62.9	17.9	*0.1*	0.53	16.4	0	97.92		
M8-c13	64.6	18.6	0.49	0.63	16.2	0.1	100.64		
N3-c2c	60.6	16.8	*0.02*	0.30	15.5	0.0	93.22		
N3-c2r	63.4	18.0	0	0.53	16.6	0.2	98.75	925	119
N3-c5	64.5	18.8	*0.11*	0.76	16.2	0.1	100.37		

	SO3	BaO	SrO	Na2O	Al2O3	Total
d.l. (wt.%)	0.3	0.6	0.6	0.13	0.12	
std.dev	8%	5%	79%	13%	22%	
M8-c3	34.3	65.4	0.8	0.13	0.53	101.1
M8-c4	33.6	65.0	1.1	0.15	0.53	100.5
M8-c5	34.6	64.9	*0.3*	0.27	0.50	100.6
M8-c6	35.1	64.7	1.1	0.26	0.46	101.7
M8-c7	34.5	65	1.0	0.21	0.44	101.2
M8-c8c	35.4	64.4	1.0	0.16	0.51	101.5
M8-c8r	33.9	64.9	0.9	0.13	0.56	100.4
M8-c9	33.9	64.5	1.2	*0.1*	0.50	100.3
M8-c10	34.5	64.5	0.5	0.12	0.58	100.2
M8-c11	33.8	64.2	0.6	0.25	0.57	99.4
M8-c12	34.8	66.6	*0.4*	*0.1*	0.56	102.4
M8-c13	34.4	64.4	1.7	0.15	0.57	101.1
N3-c2c	34.4	64.2	0.7	0.17	0.61	100.1
N3-c2r	33.8	64.6	0.8	0.3	0.51	99.9
N3-c4c	33.0	66.5	*0.0*	0.40	0.48	100.5
N3-c4r	34.5	62.6	1.8	0.24	0.53	99.7
N3-c5	35.0	64.0	1.4	0.13	0.53	101.1
N3-c6c	31.9	67.2	0.6	0.31	0.54	100.6
N3-c6r	32.1	65.9	1.1	0.21	0.58	99.9
N3-c8c	34.0	64.4	0.9	0.28	0.57	100.2
N3-c8r	34.4	63.8	1.8	0.18	0.56	100.7
N3-c9c	33.3	64.9	0.6	0.23	0.63	99.7
N3-c9r	34.6	64.8	1.1	0.14	0.49	101.1

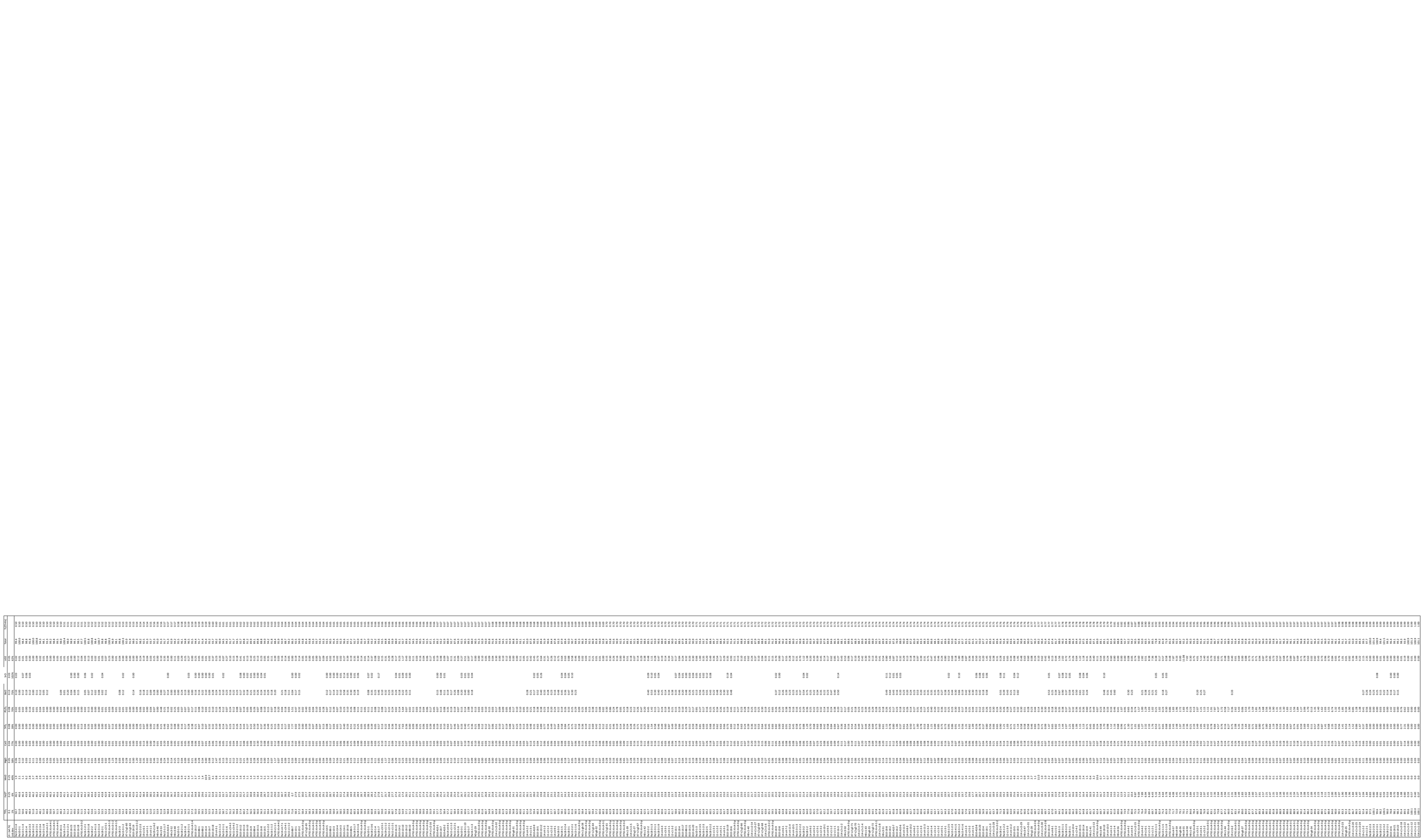

N° 9628	position	Redox	SPPg (c/s)	U-XRF (ppm)	U_ICP (ppm)	counted mass (g)	time (h)	[U] (ppm)	un.	[Ra] (ppt)	un.
A-6	*limb*	**R**	2500	7848	14290	34.9	9	14020	624	3164	410
A-8	*redox front*	**R**	420	335	340	87.3	5	388	43	1101	73
A-10	*redox front*	**R**	700	1552	1474	176	4	1641	82	915	81
B-8	*redox front*	**O**	160	35	18	30.5	73	39	16	231	15
B-12	*limb*	**R**	170	1475	1529	37	17	1513	76	416	49
B-13	*clay barrier*	**R**	120	71	20	70	62	18	7	20	2
E-6	*unaltered reduced sandstone*	**R**	100	10	n.d.	341	19	14	4	8	2
E-7	*limb*	**R**	400	1792	n.d.	343	14	1394	62	478	51
E-10	*mineralized front*	**R**	240	918	n.d.	164	4	694	34	204	23
E-13	*limb*	**R**	1200	3600	n.d.	534	4	2405	110	967	96
F-5	*mineralized front*	**R**	370	2055	n.d.	77.4	5	3106	219	790	97
F-8	*mineralized front*	**R**	650	4554	n.d.	164	3	2838	136	940	101
F-9	*limb*	**R**	450	2669	n.d.	224	3	897	51	436	41
G-10	*mineralized front*	**R**	840	3019	3319	175	4	5600	253	1644	187
G-11	*oxydized lens*	**O**	170	11	n.d.	64.5	62	43	11	391	24
G-15	*mineralized front*	**R**	350	3572	3864	53	13	3313	151	1020	114
G-16	*unaltered reduced sandstone*	**R**	100	22	21	65.1	35	25	6	12	1
H-8	*limb*	**R**	850	3484	3759	62.2	17	1043	53	490	49
H-9+10	*mineralized front*	**R**	1250	~4000	~5800	106	25	4867	211	1608	174
H11	*limb - clay barrier*	**R**	260	809	n.d.	243	13	1450	65	323	47
H-12	*limb - clay barrier*	**R**	160	38	35	35.9	105	45	12	113	8
I-6	*nose - reduced zone*	**R**	230	81	81	279	14	959	43	207	28
I-7	*nose - reduced zone*	**R**	360	97	84	194	15	144	10	80	8
I-8+9	*nose - reduced zone*	**R**	225	~2500	2122 (I8)	189	8	1714	79	793	78
I-10	*nose - reduced zone*	**R**	150	288	213	41.3	20	163	20	108	11
I-11	*nose - reduced zone*	**R**	110	33	38	194	34	39	6	29	4
I-12	*clay barrier*	**R**	100	27	23	43.5	120	33	9	12	1
J-11	*unaltered reduced sandstone*	**R**	90	n.d.	9	324	7	10	1	4	1
J-12	*nose - reduced zone*	**R**	230	1415	1174	173	6	2046	95	466	68
J-13	*nose - reduced zone*	**R**	140	524	465	293	8	282	16	81	11
J-14	*nose - reduced zone*	**R**	120	9	18	18.4	111	27	21	38	3
L-5	*nose - reduced zone*	**R**	100	9	n.d.	197	76	10	2	21	2
L-6	*nose - reduced zone*	**R**	140	13	18	204	39	24	6	116	7
L-7	*nose - reduced zone*	**R**	130	253	227	32.8	24	248	25	119	14
L8	*unaltered reduced sandstone*	**R**	90	15	13	74.7	19	30	11	8	4
M-7	*mineralization lens reduced zone*	**R**	400	4269	4566	25.6	17	4517	206	770	136
M-8	*mineralization lens reduced zone*	**R**	120	68	112	241	13	98	8	31	4
M10	*unaltered reduced sandstone*	**R**	120	23	27	54.1	138	30	7	35	3
M11	*unaltered reduced sandstone*	**R**	100	14	10	95.8	34	16	5	13	1
O-4	*mineralization lens reduced zone*	**R**	340	1285	1306	155	3	1384	72	354	50

N° 9628	position	Redox	^{234m}Pa (Bq/g)	un.	^{230}Th (Bq/g)	un.	^{226}Ra (Bq/g)	un.	^{226}Ra/^{238}U	un.	^{238}U/^{230}Th	un.	^{230}Th/^{226}Ra	un.
A-6	*limb*	**R**	173	8	132	13	116	15	0.7	0.1	1.3	0.1	1.1	0.2
A-8	*redox front*	**R**	4.8	0.5	66	7	40	3	8.4	1.1	0.07	0.01	1.6	0.2
A-10	*redox front*	**R**	20	1	14	2	33	3	1.7	0.2	1.4	0.2	0.4	0.1
B-8	*redox front*	**O**	0.5	0.2	9.2	0.9	8.4	0.5	18	7	0.05	0.02	1.1	0.1
B-12	*limb*	**R**	19	1	20	2	15	2	0.8	0.1	1.0	0.1	1.3	0.2
B-13	*clay barrier*	**R**	0.22	0.08	0.35	0.08	0.74	0.06	3.4	1.3	0.6	0.3	0.5	0.1
E-6	*unaltered reduced sandstone*	**R**	0.17	0.04	0.24	0.05	0.29	0.07	1.7	0.6	0.7	0.2	0.8	0.3
E-7	*limb*	**R**	17	1	15	2	17	2	1.0	0.1	1.2	0.1	0.8	0.1
E-10	*mineralized front*	**R**	8.6	0.4	5.4	0.7	7.5	0.9	0.9	0.1	1.6	0.2	0.7	0.1
E-13	*limb*	**R**	30	1	25	3	35	4	1.2	0.1	1.2	0.1	0.7	0.1
F-5	*mineralized front*	**R**	38	3	33	3	29	4	0.8	0.1	1.2	0.1	1.1	0.2
F-8	*mineralized front*	**R**	35	2	48	5	34	4	1.0	0.1	0.7	0.1	1.4	0.2
F-9	*limb*	**R**	11	1	11	1	16	1	1.4	0.2	1.0	0.1	0.7	0.1
G-10	*mineralized front*	**R**	69	3	59	6	60	7	0.9	0.1	1.2	0.1	1.0	0.1
G-11	*oxydized lens*	**O**	0.53	0.14	0.35	0.08	14	1	27	7	1.5	0.5	0.02	0.01
G-15	*mineralized front*	**R**	41	2	42	4	37	4	0.9	0.1	1.0	0.1	1.1	0.2
G-16	*unaltered reduced sandstone*	**R**	0.30	0.08	0.42	0.08	0.44	0.04	1.5	0.4	0.7	0.2	1.0	0.2
H-8	*limb*	**R**	13	1	11	1	18	2	1.4	0.2	1.2	0.1	0.6	0.1
H-9+10	*mineralized front*	**R**	60	3	37	4	59	6	1.0	0.1	1.6	0.2	0.6	0.1
H11	*limb - clay barrier*	**R**	18	1	18	2	12	2	0.7	0.1	1.5	0.3	1.0	0.1
H-12	*limb - clay barrier*	**R**	0.55	0.15	0.6	0.1	4.1	0.3	7.5	2.1	0.9	0.3	0.15	0.03
I-6	*nose - reduced zone*	**R**	11.8	0.5	10	1	7.6	1.0	0.6	0.1	1.2	0.1	1.3	0.2
I-7	*nose - reduced zone*	**R**	1.8	0.1	1.4	0.2	2.8	0.3	1.6	0.2	1.3	0.2	0.5	0.1
I-8+9	*nose - reduced zone*	**R**	21	1	21	2	28	3	1.4	0.2	1.0	0.1	0.7	0.1
I-10	*nose - reduced zone*	**R**	2.0	0.3	1.8	0.3	3.8	0.4	2.0	0.3	1.1	0.2	0.4	0.1
I-11	*nose - reduced zone*	**R**	0.48	0.08	0.39	0.07	1.1	0.1	2.2	0.5	1.2	0.3	0.4	0.1
I-12	*clay barrier*	**R**	0.41	0.11	0.38	0.09	0.44	0.05	1.1	0.3	1.1	0.4	0.9	0.2
J-11	*unaltered reduced sandstone*	**R**	0.12	0.01	0.19	0.02	0.15	0.02	1.2	0.2	0.7	0.1	1.3	0.2
J-12	*nose - reduced zone*	**R**	25	1	22	2	17	2	0.7	0.1	1.2	0.1	1.3	0.2
J-13	*nose - reduced zone*	**R**	3.5	0.2	3.8	0.4	2.9	0.4	0.8	0.1	0.9	0.1	1.3	0.2
J-14	*nose - reduced zone*	**R**	0.3	0.3	1.1	0.2	1.4	0.1	4.3	3.5	0.3	0.3	0.8	0.1
L-5	*nose - reduced zone*	**R**	0.13	0.03	0.34	0.04	0.78	0.06	6.0	1.5	0.4	0.1	0.4	0.1
L-6	*nose - reduced zone*	**R**	0.3	0.1	0.6	0.1	4.2	0.3	14	3.4	0.5	0.2	0.13	0.03
L-7	*nose - reduced zone*	**R**	3.1	0.3	3.7	0.4	4.4	0.5	1.4	0.2	0.8	0.1	0.8	0.1
L8	*unaltered reduced sandstone*	**R**	0.4	0.1	n.d.	n.d.	0.3	0.1	0.8	0.5	n.d.	n.d.	n.d.	n.d.
M-7	*mineralization lens reduced zone*	**R**	56	3	56	6	28	5	0.5	0.1	1.0	0.1	2.0	0.4
M-8	*mineralization lens reduced zone*	**R**	1.2	0.1	1.2	0.2	1.1	0.2	0.9	0.1	1.0	0.1	1.1	0.2
M10	*unaltered reduced sandstone*	**R**	0.4	0.1	1.0	0.1	1.3	0.1	3.5	0.9	0.4	0.1	0.8	0.1
M11	*unaltered reduced sandstone*	**R**	0.20	0.06	0.22	0.05	0.49	0.04	2.5	0.7	0.9	0.3	0.4	0.1
O-4	*mineralization lens reduced zone*	**R**	17	1	17	2	13	2	0.8	0.1	1.0	0.1	1.3	0.2